平成 29 年度 博士論文

Geology and geochemical characteristics of the Xiajinbao Au deposit in Hebei Province, China

中国河北省下金宝金鉱床の地質と地球化学的特徴

2018 年 3 月

Li Hongbin

李 宏斌

博士工 9515005

秋田大学大学院

工学資源学研究科（博士後期課程）

資源学専攻

Abstract

The North China Craton is one of important regions for precious metal resources in China. Eastern Hebei Province in the craton has a long history regarding supply of gold for royal dynasties for thousands of years. The exploration of gold resource has been focused on the granite porphyry for a long time in the North China Craton. The Xiajinbao gold deposit is located in Yanshan district of the Craton. It is located in the northeast part of Beijing, and about 210 km away from the Beijing. Granite porphyry (Ilmenite-series) and diorite are present in the Xiajinbao deposit. The orebody predominantly is hosted in the granite porphyry. In the Xiajinbao deposit, previous researches also suggested that the granite porphyry is the source of the gold mineralization based on the similar ages between the granite porphyry and mineralization. However, the gold mineralization of the Xiajinbao deposit is thought to be formed by oxidized magmatism such as diorite based on the data in this study.

The orebodies of the Xiajinbao deposit, composed of aggregates of large number of veins and veinlets having width from 5cm to 1mm, occur mainly in the granite porphyry within an area of 800m by 300m. Base on cross-cutting relationships, the veins are classified into pyrite-quartz veins, pyrite-chalcopyrite quartz veins, and sphalerite-galena quartz veins from earlier to later. Pyrite quartz veins are composed of large amounts of quartz and pyrite with trace amounts of chalcopyrite and electrum. Pyrite-chalcopyrite quartz veins are composed of large amounts of quartz, pyrite, and chalcopyrite. Sphalerite-galena quartz veins are composed of large amounts of quartz, sphalerite and galena, small amounts of pyrite and chalcopyrite, and trace amounts of native bismuth, tetrahedrite and electrum. Quantity of electrum in sphalerite-galena quartz veins are larger than that of electrum in the pyrite quartz vein and pyrite-chalcopyrite quartz veins.

The granite porphyry consists of quartz, orthoclase, plagioclase and biotite as phenocrysts with trace amounts of ilmenite, zircon, rutile and apatite without magnetite. On the other hand, the diorite consists of plagioclase, amphibole and biotite with small amounts of apatite, magnetite, hematite, ilmenite and pyrite. The magnetic susceptibility of granite porphyry is generally

lower than 0.1×10^{-3} SI unit while the diorite have much higher magnetic susceptibility from 30 to 60 $\times10^{-3}$ SI unit in the Xiajinbao deposit. The igneous activity of Xiajinbao mining area is characterized by bimodal igneous activity. The distribution of diorite dike accords with the distribution in areas having high Au content. Au rich part (approx. 220ppm) is present near the diorite dike in the underground workings of the Xiajinbao deposit. These geological features indicate that mineralization has relationship with those diorite dikes in space.

The SiO_2 and TiO_2 contents of granite porphyry are around 70 wt% and 0.2 wt%, respectively. The Al_2O_3 contents of granite porphyry range from 13.9 to 14.3 wt%. The T-Fe_2O_3 contents of granite porphyry range from 1.9 to 2.5 wt%. The Na_2O and K_2O contents of granite porphyry range from 2.3 to 2.9 wt% and 4.6 to 6.1 wt%, respectively. The aluminum saturation index of granite porphyry ranges from 1.12 to 1.28. These features suggest that the granite porphyry belongs to the ilmenite-series granitic rocks. The granite porphyry was formed by reduced magma. On the other hand, the SiO_2 and Al_2O_3 contents of diorite dikes are 49.1 to 51.1 wt% and 13.7 to 16.3 wt%, respectively. The TiO_2 content of diorite dikes ranges from 1.0 to 3.1 wt%. The T-Fe_2O_3 content of diorite dikes is 7.3 to 11.5 wt%. The Na_2O and K_2O contents of diorite dikes are 3.3 to 4.1wt% and 2.4 to 2.9wt%, respectively. The Zr/TiO_2 ratios of granite porphyry and quartz porphyry dikes are both around 770 while the Zr/TiO_2 ratios of diorite dikes in the underground and outcrop are approximately 150 and 60. These ratios indicate that the characteristics of magma of granite porphyry and quartz porphyry dikes are similar. On the other hand, these are different from the characteristics of magma of diorite dikes.

The sulfur fugacity of sphalerite-galena quartz vein is estimated to be around 10^{-12} atm. The formation environment of the sphalerite-galena quartz vein of the Xiajinbao deposit is similar to the environment of zoned base metal veins associated with oxidized magma. The $\delta^{34}S$ values of sulfide minerals of the Xiajinbao deposit range from -3 to +8 ‰ with a mode of +4 ‰. The distribution of sulfur isotopic ratios of the sulfide minerals of the Xiajinbao deposit are similar to the distribution of $\delta^{34}S$ of ores associated with oxidized magmas. The formation environment of gold-bearing sphalerite-galena-quartz veins of the Xiajinbao deposit is different

from formation environment of hydrothermal activities associated with reduced granitic magma. The oxygen and hydrogen isotopic ratios of hydrothermal solution in equilibrium with quartz from the sphalerite-galena quartz vein range from +3.3 to +5.5 ‰ and -38 to -41‰, respectively. The oxygen and hydrogen isotopic ratios suggest hydrothermal solution of the pyrite quartz veins, pyrite-chalcopyrite quartz veins and sphalerite-galena quartz veins was magmatic origin.

Based on the geological, geochemical and isotopic data, Au mineralization of the Xiajinbao deposit is thought to have intimate relation with oxidized magma such as diorite.

Table of contents

Chapter 1 Introduction

1.1 Outline of gold deposit in North China Craton

On the basis of the different geodynamic environment, tectonic unit and geological evolution, gold deposits in China have been classified into 5 metallogenic domains and thirty-seven metallogenic regions (Zhang et al., 2014). In the north China Craton, based on the distribution of early Precambrian rocks, and through integrated geological, geochronological and geophysical information, at least six micro-continental blocks have been identified within the North China Craton (Fig. 1). These micro blocks were amalgamated by 2.5 Ga, defining the fundamental Precambrian architecture of the North China Craton (Bai et al., 1993; Wu et al., 1998; Zhai and Santosh, 2011, 2013; Zhai et al., 2000, 2005). Between the micro blocks and the margin of the North China Craton are the weak zones. These positions are favorite for the major tectonic, magmatic and metallogenic events. Gold is one of the most important mineral resources in the North China Craton. Gold deposits in the NCC are dominantly distributed along the central domains of the eastern, southern and northern margins of the

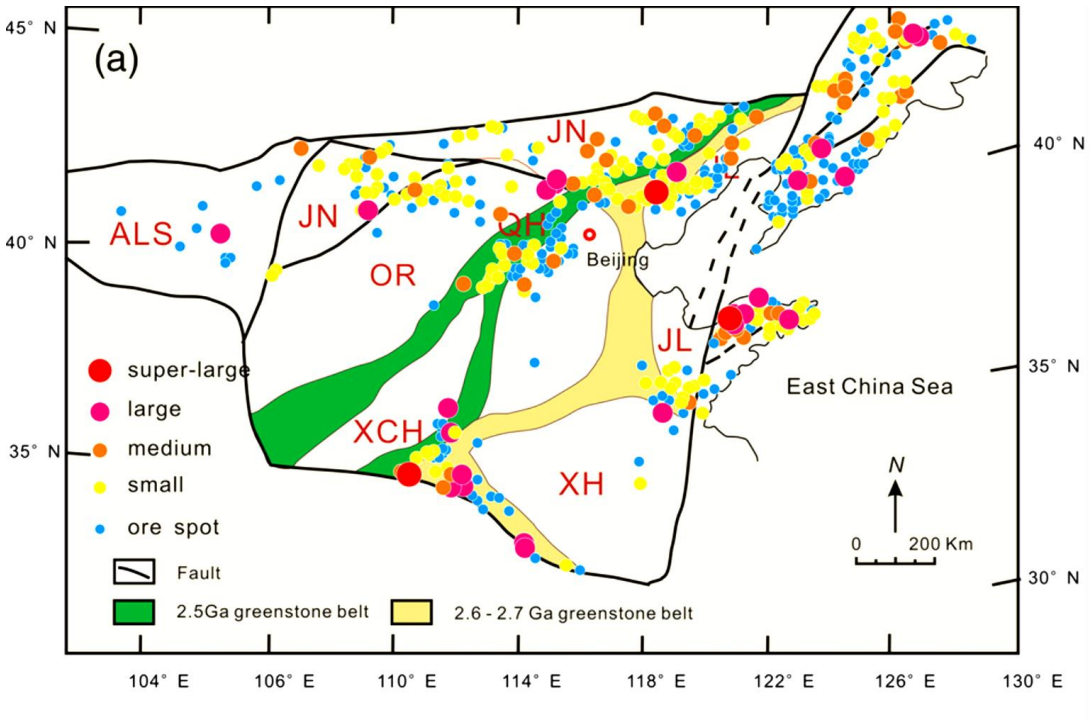

Fig. 1 Locations of ore deposits in the North China Craton. ALS = Alashan block, JN = Jining block, OR = Ordos Block, QH = Qianhuai block, XCH = Xuchang or Fuping block, XH = Xuhuai, and JL = Jiaoliao block. Modified from Li and Santosh (2014).

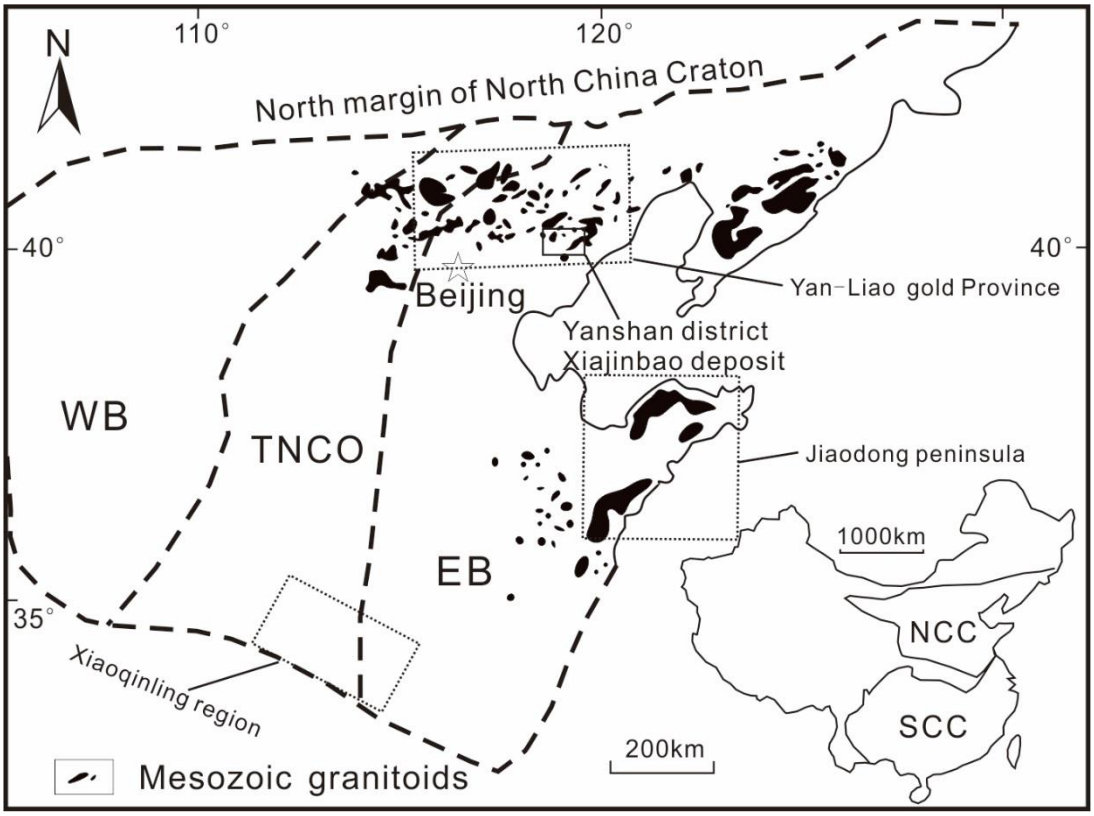

Fig. 2 The location map of Yan-Liao gold field. Distribution of Mesozoic granitoids in the North China Craton is also shown. NCC, SCC, WB, TNCO and EB denote the North China Craton, South China Craton, Western Block, Trans-North China Orogen and Eastern Block, respectively (Modified from Zhao et al., 2001).

craton. The major gold deposits are found in the Jiaodong peninsula (eastern North China Craton), the Xiaoqinling region (southern North China Craton), and the Jibei region (Fig. 2) (northern North China Craton). These deposits combined have a total proven reserve of calculated 2500 t Au. The Jiaodong peninsula has long been known to host the largest cluster of gold deposits in China, and has been the major production in the country. The Xiaoqinling region hosts the second largest gold cluster (Li and Santosh, 2014). The northern margin of the North China craton is well- endowed with gold, containing approximately 900 gold deposits and occurrences that are estimated to host approximately 20% of China's 4,500 t gold resource (Nie 1997a; Miller at al., 1998; Zhou et al., 2002). In the northern margin of North China Craton, three main gold provinces are defined. From west to east, they are termed the Daqinshan, Yan-Liao, and Changbaishan gold provinces. In the Yan-Liao gold Province (from Zhangjiakou district to Chifeng district), the Jinchangyu (Yanshan district) quartz-vein gold deposit (Song et al., 2014), the Xiaoyingpan quartz-vein gold deposit (Qiu et al., 1997), and the Dongping (Zhangjiakou district) quartz-vein–altered–fracture transition type gold deposit (Miao et al., 2002), and they are among the large-super large gold deposits. In the EW-trending Yan-Liao gold Province, about 1,000 t of gold has been obtained (Hart et al., 2002).

1.1.1 Distribution of gold deposit in Yan-Liao gold Province

The Yan-Liao gold province in the north and northeast of Beijing includes three districts defined by clusters of gold occurrences named in Zhangjiakou, Yanshan, and Chifeng (Fig. 3). The Yan-Liao gold province stretches across northern Hebei and western Liaoning provinces and parts of southern Inner Mongolia. The gold occurrences in the Yan-Liao gold province are within uplifted blocks of Middle Archean gneiss, amphibolite, and granulite. These terranes are overlain by Mesoproterozoic to Neoproterozoic volcano-sedimentary rocks. Caledonian (Cambrian to Silurian), Variscan (Devonian to Permian), and Yanshanian (lower Jurassic to lower Cretaceous) plutonic suites are widespread and locally host some of the gold deposits (Chen and Dong, 1993).

Highly metamorphosed Archean and Paleoproterozoic rocks are widely outcropped and have an outcrop area around 9.8% of the total North China Craton. These basements were also covered or surrounded by less metamorphosed Mesoproterozoic, Neoproterozoic and Paleozoic volcano-sedimentary rocks. These metamorphosed rocks occupy 22.6% area of the total North China Craton (Xie et al., 1996). Most of these intrusion-related gold deposits occur within the Precambrian terrain, and show an intimate spatial and temporal relationship with Hercynian and Yanshanian intrusions. The gold deposits in Yan-Liao gold field are mainly distributed in Zhangjiakou district, Chifeng district and Yanshan district (Hart et al., 2002). Approximately 30% of the region is underlain by uplifted blocks of high-grade Archean and Paleoproterozoic metamorphic rocks, with about 70% of the gold mineralization in these rocks, and the remainder in late Paleozoic to Mesozoic granitoids that were emplaced into these same basement blocks (Nie, 1997b; Qiu et al., 1993; Qiu et al., 1995).

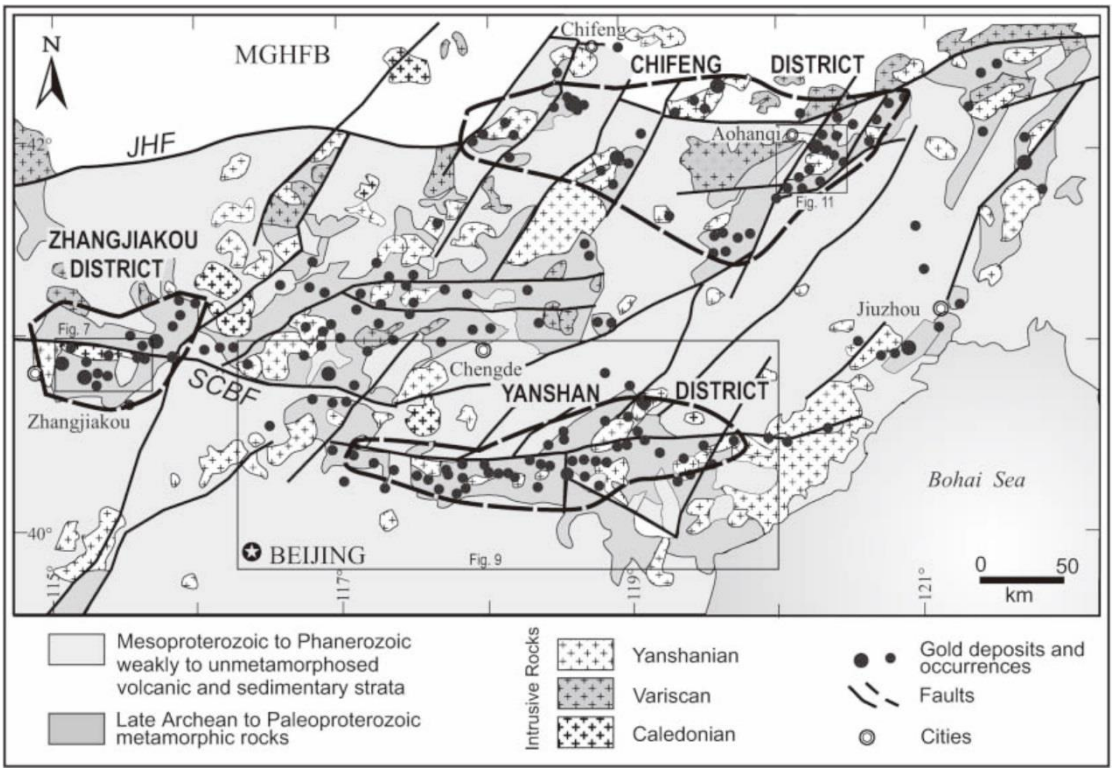

Fig. 3 Generalized geology of the Yan-Liao gold province in the northern North China craton showing the distribution of gold occurrences and deposits with respect to the Precambrian basement rocks and the Phanerozoic granitoid intrusions. General localities of mining districts discussed in the text are also shown. Geology modified from Hart et al. (2002) after Chen and Dong (1993). MGHFB Mongolian–Great Hinggan Fold Belt; NCC North China craton; JHF Junggar–Hegenfault; SCBF Shangyi–Chicheng–Beipiao fault.

1.1.2 Genesis of gold deposits in North margin of North China Craton

The common occurrence of basement rock hosted gold ores led many workers to suggest that most of the deposits are Archean in age (e.g., Yang, 1996; Xu et al. 2000), or that mineralization may be younger, but that the gold was derived directly from inherently gold-rich Late Archean rocks (e.g., Qiu et al.1993; Cai et al. 1996; Zhang et al. 1999)

The region hosts several suites of late Paleozoic to Cretaceous felsic plutons. However, because some of the gold deposits are hosted within these granitoids, other workers have suggested that the ores may be magmatic in origin (e.g., Sillitoe and Thompson1998). Plutons of Yanshanian (middle to late Mesozoic) age have also been suspected as being important mineralizing agents because of their quartz-rich nature and spatial relationship with deposits in the eastern part of the belt (Trumbull et al. 1992). In particular, intrusion-related gold deposits occurring within the North China Craton and along its marginal belts are classified into three groups according to their host rocks: (1) gold deposits in felsic intrusions, including calc-alkaline granitic intrusions (e.g, the Yu'erya, Anjiayingzi, Linglong, and Jiaojia deposits) and

breccia pipes (e.g, the Chenjiazhangzi and Qiyugou deposits); (2) gold deposits in alkaline intrusions (e.g, the Wulashan, Donghuofang, Dongping, Hougou and Guilaizhuang deposits) and (3) gold deposits in ultramafic intrusions (e.g, the Jinjiazhuang gold deposit) (Nie, 1997a, b; Nie, 1998; Nie et al., 2004). These intrusion-related gold deposits were thought to be products of fluid exsolved from the magma.

1.1.3 Previous work and outstanding questions

Gold is a widely distributed element occurring almost in all types of rocks. Nevertheless, as its abundance is very low (~4 ppb), it requires high enrichment (~1000 to 4000 times of the average crustal Au value) before forming an ore deposit. One or more geological processes, including sedimentation, volcanism, magmatic activities, deformation and metamorphism, may play important role during the mobilization, transportation and deposition of gold (Xu et al., 1992). Previous study provides fruitful and meaningful results in the Yanshan district. The fluid inclusion, hydrogen and oxygen isotope studies suggest that ore forming fluid of most the gold deposits in Yanshan district was mainly magmatic fluid origin while some gold deposits show different meteoric influence (Luan and Yu, 1995; Wang et al., 2003; Zhang et al., 2017). The tectonic stress field study suggests that the deformation and fault system provide the space for magma emplacement and mineralization (Lei et al., 1995a, b). The sulfur isotope data suggest that the calc-alkaline and alkaline intrusions in the vicinity of the gold occurrences of the North China Craton show positive $\delta^{34}S$ values from 1 to 7‰. The sulfide separates (pyrite, galena, chalcopyrite and pyrrhotite) from gold deposits hosted by calc-alkaline granitoid and alkaline intrusive rocks are ranged from -3.3 to 14‰ and -14.3 to 6‰ (Nie et al., 2004). Some researchers suggest that these $\delta^{34}S$ values are similar to that of pyrite separates from many porphyry copper deposits -5.5 to 6.5‰ (Deng, 2014; Ye, 2013). Second interpretation is the $\delta^{34}S$ values may gradually become isotopically lighter as the fluid is oxidized or mixing of fluids with different isotopic composition (Ohmoto, 1986). Third interpretation is that magmatic fluids interacted with isotopically depleted wall rocks such as the Precambrian metamorphic rocks which generated $\delta^{34}S$ values from -20 to -2‰. The lead isotope study suggests that no matter in what tectonic positions the ore deposits occur, the ore-forming materials came from the same source of mantle while some deposits show characteristics of mixing of lower crust (Wang et al., 2003). However, the role of intrusive rocks during the mineralization still needs to be discussed carefully. In the Xiajinbao mining area, the gold mineralization is mainly host in the granite porphyry while some quartz porphyry dikes and diorite dikes are present in the granite porphyry. The age of granite porphyry determined by fission track method regarding apatite and zircon is estimated to be 103 to 154 Ma (Yuan et al.,

1999). The age for the granite porphyry and quartz porphyry dikes determined by zircon U-Pb method is 158 to 163 Ma (Li et al., 2016; Zhang et al., 2016; Zou et al., 2016). The age for the mineralization determined by Zou et al. (2016) on one molybdenite sample using Re-Os dating technology is 163 Ma. On the other hand, the Precambrian metamorphic rock (gneiss) and sedimentary rock (sand stone) in the Xiajinbao mining area have a high gold background value of 0.029 ppm and 0.018 ppm, respectively. These values are 7 and 4 times higher than the Clarke value, respectively. On the base of above discussion, previous researches thought that gold mineralization have intimate relation to the granite porphyry and some of the ore-forming materials may extracted from the wall rock (Tang et al., 2009; Ye, 2013; Zhang et al., 2017). In this study, the granite porphyry in the Xiajinbao deposit shows an ilmenite-series granitoid feature. This kind of granitoid is difficult to provide ore-forming materials for gold mineralization.

1.2 Outline of study area

The geology of Yanshan District is composed of Archean basement rocks, Mesoproterozoic, Neoproterozoic, Phanerozoic and Cenozoic strata in ascending order (Fig. 4). The Archean basement consists of tonalite-trondhjemite-granodiorite gneisses, migmatite, amphibolite, ultramafic rocks, and banded iron formations (Santosh, 2010; Santosh et al., 2013; Zhai, 2014; Zhao et al., 2001). The Mesoproterozoic and Neoproterozoic strata consist of medium to coarse-grained quartz sandstone, shale, dolomite and quartzite in ascending order. The Phanerozoic strata are mainly Mesozoic sedimentary and volcanic rocks. There is an

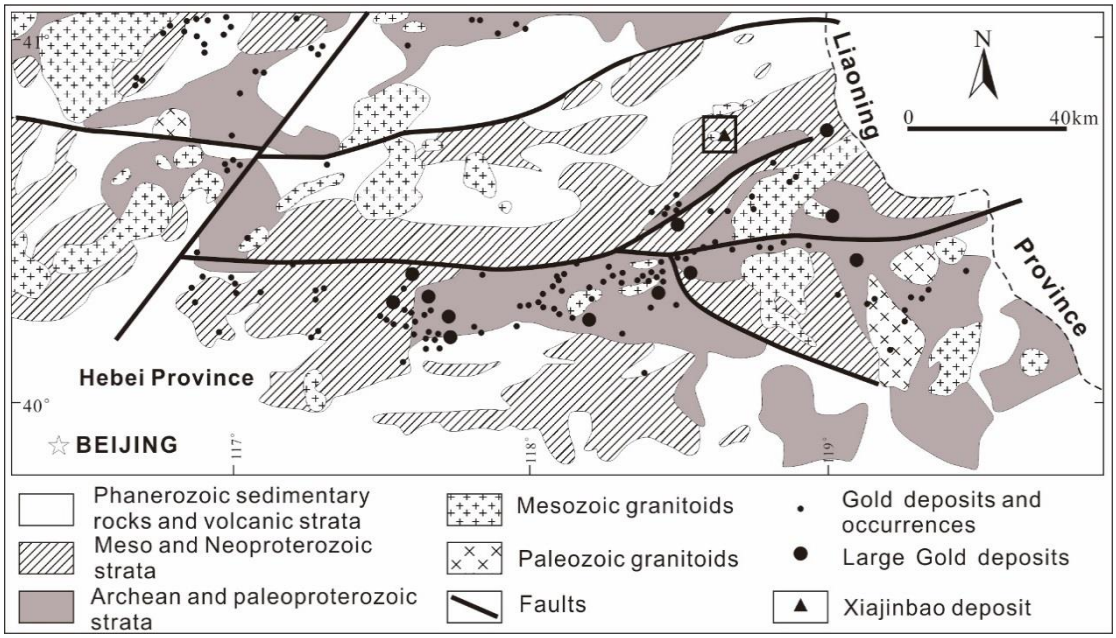

Fig. 4 Simplified geological map of the Yanshan district of east portion of Yan-Liao gold field in east Hebei Province (Modified from Hart et al. 2002). The location of the Xiajinbao deposit is shown in this map.

unconformity between Mesoproterozoic and Mesozoic strata. The Mesozoic strata consist dominantly of Jurassic volcanic rocks such as andesite lava and andesitic breccia. The strata of Cenozoic are mainly Quaternary sediments. The Mesozoic intrusive rocks in Yanshan District consist of large amount of felsic intrusive rocks with subordinate intermediate and mafic intrusive rocks. The number of intrusive rocks decreases from the northeastern part to the central part in the district. The age of intrusive rocks also becomes younger from the northeast part to the central part in the district.

The gold deposits in Yanshan District are distributed along the east-west trending faults that are subparallel to the contact between the North China Craton and Central Asian Orogen (Liu et al., 2016).

1.3 Outline of ore deposits

The Xiajinbao gold deposit is one part of the Xiayingfang gold field. In the previous studies, researchers called the deposit Xiayingfang gold deposit. After 1990s, other deposit such as Dongliang gold deposit was found in the east of Xiayingfang gold field. The Xiajinbao gold deposit was taken over by Jinbao mining company and renamed it officially. The Xiajinbao gold deposit has a long history of exploration. Early in 1956, Hebei Geology Bureau primly found gold mineralized spot in the Xiayingfang gold field. In 1970s, the fourth geology team of Hebei Geology Bureau started geology survey on the target of iron and copper. From 1980s to 1990s, the fifth team of Hebei Geology Bureau did the general exploration, geophysical and geochemical prospecting for gold in the Xiayingfang gold field. The orebodies on the surface are distributed on the east of granite porphyry in the Xiajinbao mining area and extent to south-west in the deep portion. The orebodies distributed in an area of 800m by 300m. The general strike and dip is 30 to 40° and 40 to 80° NWW, respectively. The average grade of gold is 1.9 ppm.

1.4 Aim of study

Based on all the previous study and outstanding questions, aims of this study are summarized as follows:

1. Clarify the type of igneous activity and formation environment of the Xiajinbao deposit.
2. Clarify the relation between igneous activity and gold mineralization
3. Elucidate the gold mineralization mechanism in the Xiajinbao deposit.

Chapter 2 Methods

2.1 Field investigation

Two field investigations had been carried out in the Xiajinbao and Dongliang deposit in 2016. Geology of these two deposit was observed during the field investigation. Several route maps were sketched, type of igneous rocks were examined, the cross-cutting relationships of the gold bearing quartz veins were observed, and samples of rocks, ores from the outcrop, and drilling cores of the Xiajinbao deposit and Dongliang deposit were collected for this study. During the field investigation and route mapping, the magnetic susceptibility of igneous rocks in the Xiajinbao deposit and the Dongliang deposit were also measured at each observation point.

2.2 Observation of sample by naked eyes and microscope

Samples collected in the field were processed in Graduate School of Engineering and Resource Science, Akita University to do observation by naked eye. Thin sections and polish sections were made for microscope observation. These sections would be observed under polarized microscope to identify rock-formation minerals and opaque minerals. The textures, paragenetic sequence among minerals were also observed.

2.3 X-Ray diffraction (XRD)

The collected samples were also analysis by X-Ray diffraction to identify the minerals. The powders of the samples were made in the Graduate School of Engineering and Resource Science, Akita University. The equipment for anylsis is an XRF Rigaku MiniFlex II. The data is collected from 2°to 60°, as 2θ step scan is 0.02°at every 1 second.

2.4 Electron probe micro-analysis (EPMA)

Thin sections and polish sections were also used for EPMA analysis to identify the presence of minerals and analyse the chemical composition of minerals. The EPMA equipment used is the JEOL SUPERPROBE JXA-733 at Graduate School of Engineering and Resource Science, Akita University. The analyzed elements of sphalerite were Zn, Fe, Mn, Cd, Cu, In, Ga, and S. Acceleration voltage was 20 kV, beam current was 20 nA and diameter of the electron beam was 3-5 μm. The characteristic X-rays for measurements of concentrations were Zn Kα, Fe Kα, Mn Kα, Cd Lα, Cu Kα, In Lα, Ga Kα and S Kα. The standards for these elements were Zn metal, $CuFeS_2$, MnS, GaAs (LiF crystal), Cd and InSb (TAP crystal), respectively. All of the data were corrected with a ZAF-metal matrix correction program (Sweatman and Long, 1969).

The detection limit was 0.1 wt%.

2.5 X-Ray fluorescence (XRF)

XRF is used to determine major components of whole rock samples. The powders used for XRF analysis is finer compare to XRD analysis. The powders were fined-grained by using ethanol and dried over night at 110 ºC. After that, dried powders were heated at 900 ºC for 3.5 hours for decomposition of minerals to oxide and releasing structure water and gases. At last, the powders were mixed with fluxes and heated again at around 1000 ºC to obtain glass beads for XRF analysis. The calibration line was made every time before analyze sample. The set of Japanese rock standard JA-1, JA-2, JA-3, JB-1, JB-1b, JB-3, JG-1a, JG-2, JG-3, JGb-1, JP-1, JP-2 were used to make calibration line

2.6 Inductively couple plasma mass spectrometry (ICP-MS)

Inductively couple plasma mass spectrometry (ICP-MS) is capable of detecting trace elements at concentrations as low as one part per trillion. However, analysis by ICP-MS is also susceptible to contaminations from sample preparation. In addition, detection of some ions is interfered by other ions. The concentration of zirconium is also dependent on how the samples were prepared. In this study, about 0.1g powder of samples were digested by mixture of perchloric acid (60% $HClO_4$), hydrofluoric acid (48% HF) and nitric acid (62% HNO_3). After mixture, the samples were diluted to 1000 times by using 3% nitric acid. The diluted nitric acid was made by the mixing of 62% HNO_3 and ultra-pure water to prevent contamination. After dilute to 1000 times, samples without precipitation were confirmed to be completely diluted. Finally, the 1000 times-diluted solution samples were further diluted to 10000 times, each sample solution as a set of two: one was standard free and the other with standard. The calibration lines were made from the blank solution, sample solution and sample solution with standard. The element rhenium was used as a correction for the count of drift for the ICP_MS equipment. The procedure was described by (Sato et al., 1999).

2.7 Fluid inclusions

The fluid inclusion study is used to determine the formation temperature and salinity of the ore forming fluid. The fluid inclusions was observed on both-side polished sections for quartz. The thickness of sections were polished around 0.06mm to 0.1mm. Homogenization temperature and salinity of fluid inclusions were measured using the Linkam THMSG600 cooling-heating stage in the Key Laboratory of Nonferrous Metal Metallogenic Prediction of Chinese Ministry of Education of Central South University. Ranges of temperatures for measurement were from room temperature to 600 °C for heating and from room temperature to

-50 °C for cooling. The analytical precision of measurements of temperatures for heating experiments and that for cooling experiments were ±1 °C and ±0.1 °C, respectively. Salinity was calculated on the base of the final ice melting temperature and solubility of NaCl in water (Bodnar, 1993).

2.8 Stable isotope study

2.8.1 Oxygen and hydrogen isotopic ratios

Oxygen isotope ratios of quartz and bulk samples of altered rocks and hydrogen isotopic ratios of illite separated from the altered rocks were determined by using a mass spectrometer (Iso-Prime) in Akita University. The method used for analysis of oxygen isotope ratios was the F_2-technique (Kita and Matsubaya, 1983). The $\delta^{18}O$ values are given relative to SMOW. The analytical precision of oxygen isotope ratios was ±0.2‰. The illite was separated from the altered rocks by elutriation for determination of hydrogen isotope ratios. The purity of illite was confirmed by XRD analysis. All of the samples were composed of a large quantity of illite and a small amount of quartz. Those samples were used for measurement of hydrogen isotope ratios of illite. The method used for analysis of hydrogen isotopic ratios was the method described by Marumo et al. (1995). The analytical precision of hydrogen isotope ratios was ±1‰.

2.8.2 Sulfur isotopic ratios

The sulfur isotope ratios of pyrite and galena that coexist in sphalerite-galena quartz veins were determined. Sulfur isotope ratios of sulfide minerals were determined by using a MAT-251 mass spectrometer in Analytical Laboratory of Beijing Research Institute of Uranium Geology. The $\delta^{34}S$ values are given relative to CDT. Analytical precision was ±0.2‰.

Chapter 3 Gold mineralization of the Xiajinbao deposit

3.1 Geology of the Xiajinbao deposit

3.1.1 Stratigraphy

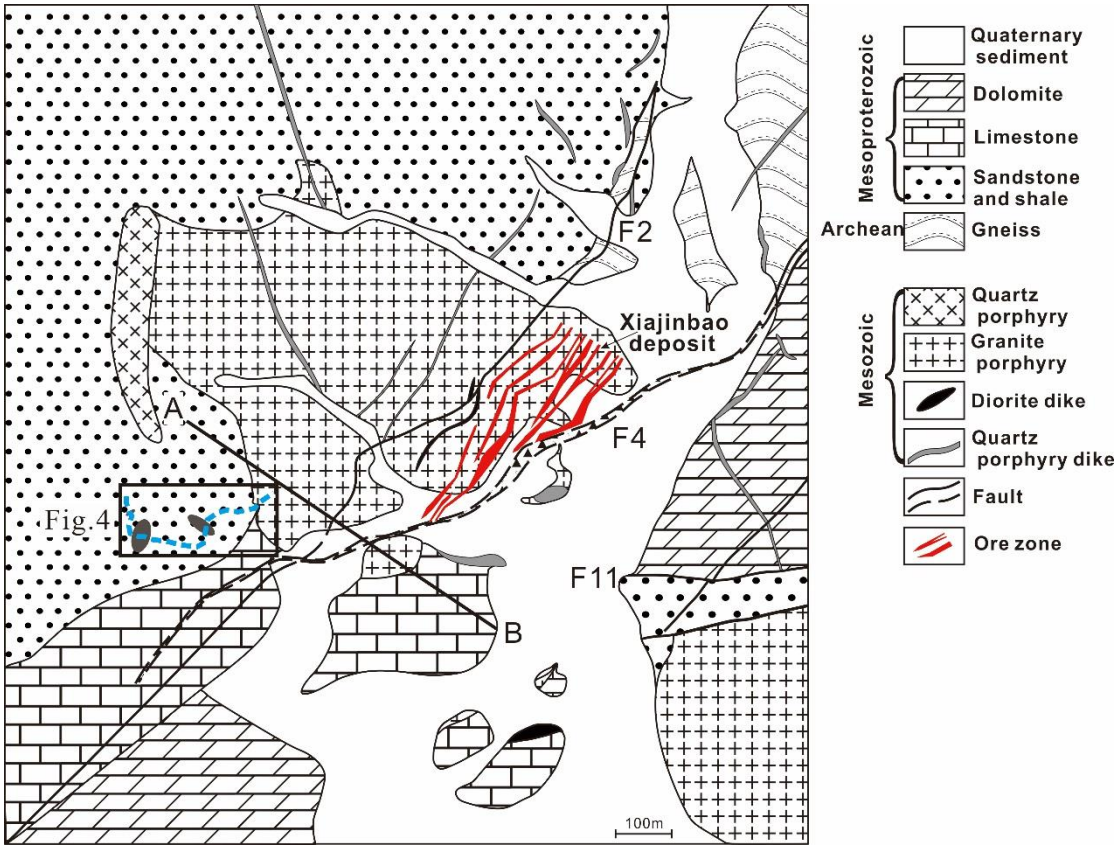

Fig. 5 Geologic map of the Xiajinbao mining area. The box shows the location of route map in Fig. 6. The A-B line corresponds to the cross-section of Fig. 7.

The oldest terrane in the Xiajinbao mining area is Archean gneiss. Mesoproterozoic terranes include Changzhougou group (Chc) sandstone, Dahongyu group (Chd) dolomite and dolomitic limestone, Gaoyuzhuang group (Chg) dolomite, limestone, and sandstone alternation in ascent sequence. These groups belong to the Changcheng Period (Claymmian). The intrusive rocks in the Xiajinbao mining area are Jurassic granite porphyry, quartz porphyry dikes and diorite dikes. Archean gneiss and Proterozoic sandstone are present in the northeastern and northern parts of the Xiajinbao mining area, respectively (Fig. 5). Proterozoic limestone and dolomite are distributed in the southern and eastern parts of the mining area (Fig. 5). Quaternary sediments cover the central part of the mining area.

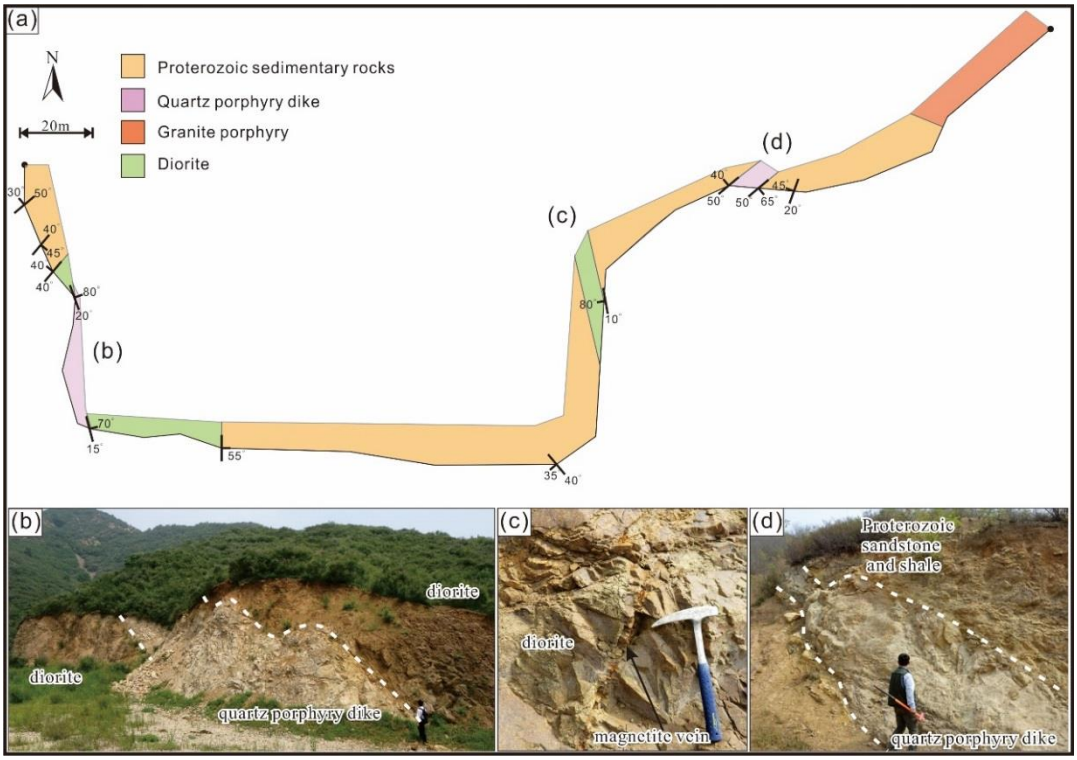

Fig. 6 (a) Route map showing cross-cutting relationships between diorite dikes and quartz porphyry dikes. (b) Picture showing the mode of occurrence that the quartz porphyry dike cut diorite dike. (c) Picture showing presence of magnetite vein in the diorite dike. (d) Quartz porphyry dike in alternation of Proterozoic sandstone and shale.

3.1.2 Intrusive rocks

Intrusive rocks in the Xiajinbao mining area are granite porphyry, quartz porphyries and diorite dikes. The granite porphyry is host rock of the Xiajinbao gold deposit and is distributed in the central part of the mining area (Fig. 5). Some diorite dikes and quartz porphyry dikes are present in granite porphyry and Proterozoic sedimentary rocks in the southern part of the granite porphyry (Figs. 6a, 6b and 6d). Some diorite dikes cut the granite porphyry in a deep part of the Xiajinbao deposit (Fig. 7). The quartz porphyry also cut diorite in the Xiajinbao mining area (Fig. 6b). Based on the cross-cutting relation, the sequence of emplacement of igneous rocks in the Xiajinbao mining area is thought to be in the order from granite porphyry, diorite dike to quartz porphyry dike (Li et al., 2018).

The granite porphyry shows a reddish color and porphyritic structure. The granite porphyry consists of quartz, orthoclase, plagioclase, and biotite as phenocrysts with small amounts of zircon, rutile and apatite (Fig. 8a). Opaque minerals are mainly pyrite and small amount of ilmenite. Quartz and plagioclase phenocrysts show a subhedral shape. The matrix of the granite porphyry is composed of fine-grained quartz and feldspar. A small amount of illite replacing plagioclase is present as altered mineral in the granite porphyry (Fig. 8b). In strongly altered granite porphyry near mineralized veins, mineral assemblage of quartz and illite

characterizes the altered granite porphyry.

Quartz porphyry dike having a gray color consists of a large amount of quartz with small amounts of plagioclase and orthoclase (Figs. 8c and 8d). The matrix of quartz porphyry is cryptocrystalline felsic minerals.

The diorite dikes of the outcrop and underground of the Xiajinbao deposit show a dark gray color. The diorite shows a massive structure and a hypidiomorphic granular texture (Fig. 8e). The mineral assemblage of diorite consists of large amounts of plagioclase and amphibole with small amounts of biotite and apatite (Fig. 8f). The size of the plagioclase of the diorite dike underground is smaller than that of plagioclase of the diorite dike in the outcrop (Fig. 8g).

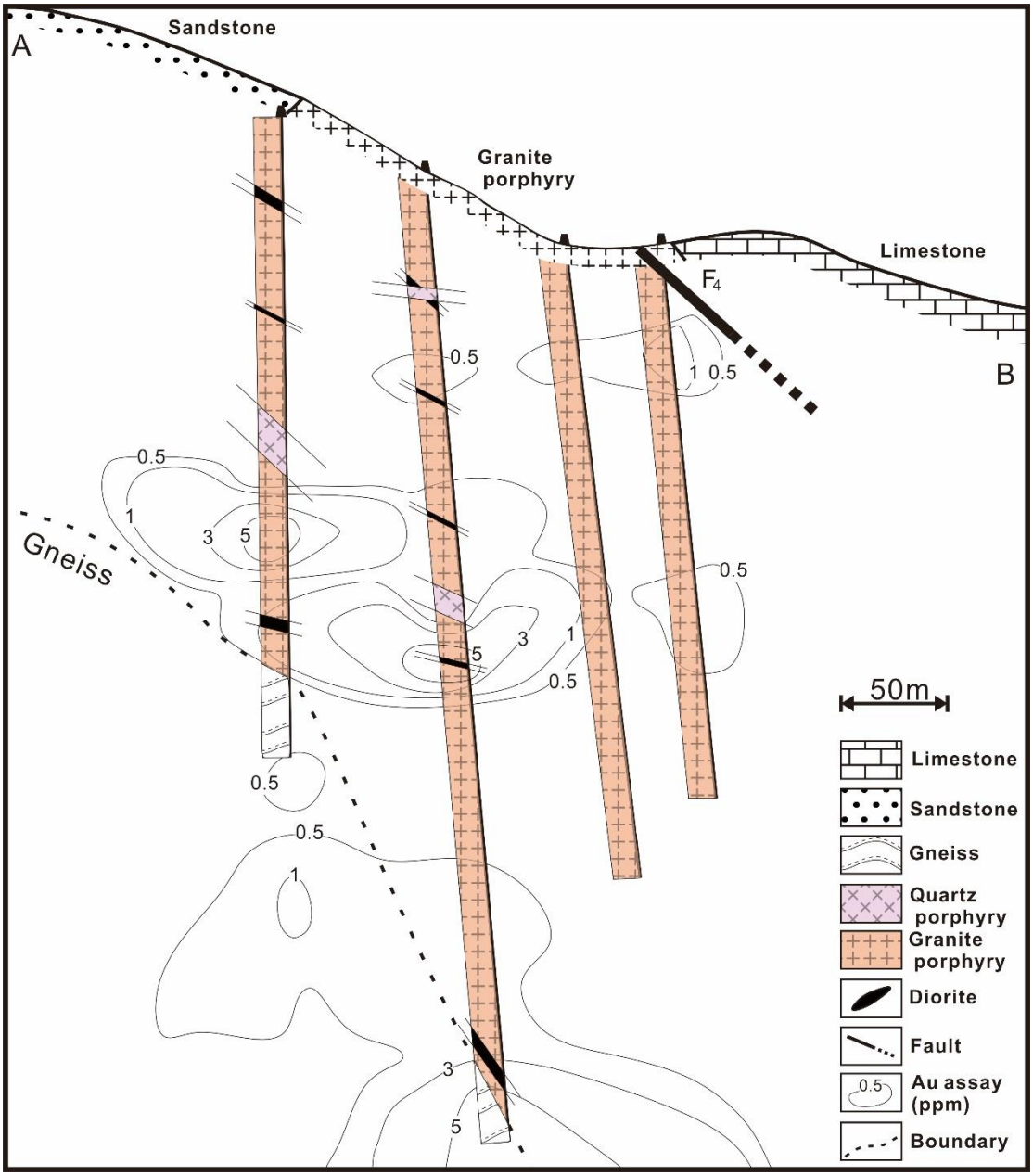

Fig. 7 Diagram showing A-B cross-section in Fig. 3 of the Xiajinbao deposit. The gold assay data is also shown. Unit of assay data is in ppm.

Opaque minerals in the diorite dike are magnetite, hematite, and pyrite. Some magnetite veins occur in the diorite dike in the outcrop (Fig. 8c). As alteration minerals, chlorite, dolomite and illite are present in some parts of the diorite dike. The degree of alteration of the diorite dike underground is stronger than that of the diorite dike in the outcrop (Fig. 8h).

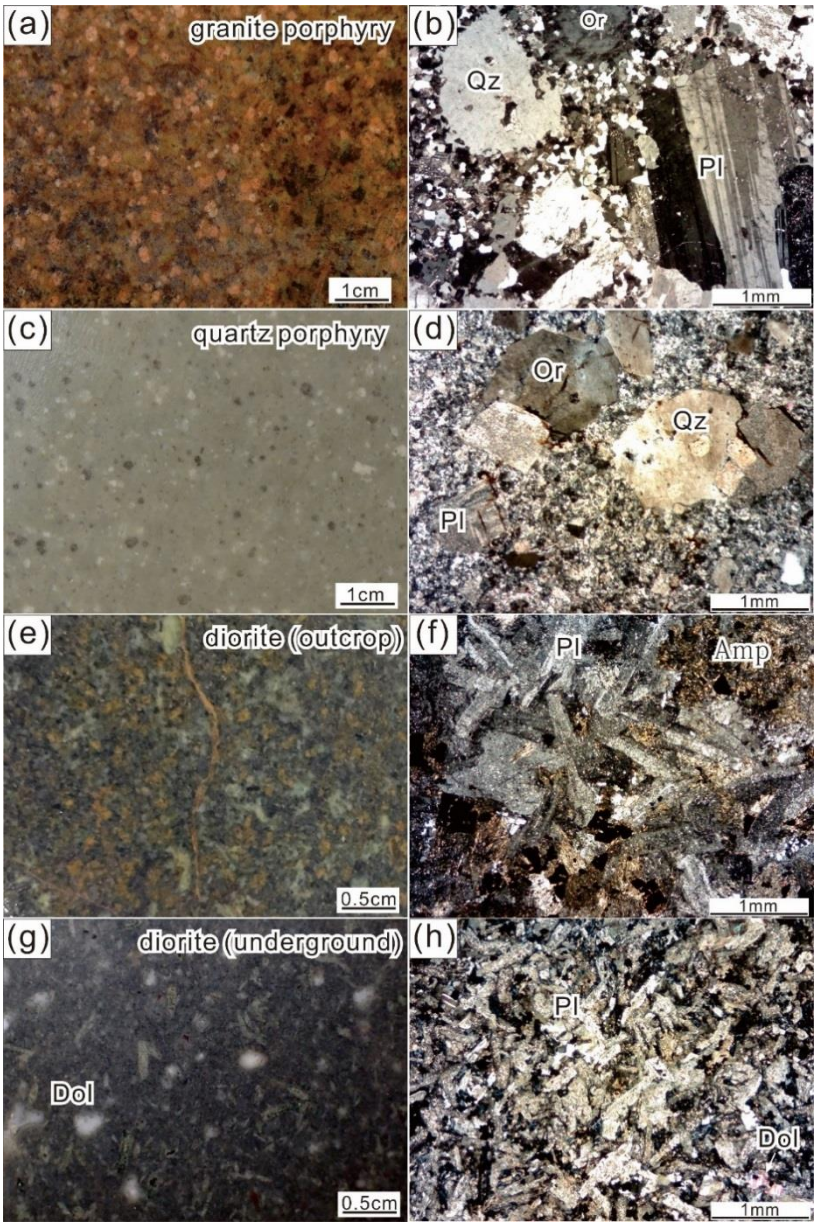

Fig. 8 Pictures showing representative rocks and photomicrographs. (a), (c), (e), (g) Pictures showing granite porphyry, quartz porphyry dike, diorite dike of outcrop, diorite dike from underground, respectively. (b), (d), (f), (h) Photomicrographs showing textures of granite porphyry, quartz porphyry dike, diorite dike of outcrop, diorite dike from underground, respectively. Abbreviations: qz: quartz, pl: plagioclase, or: orthoclase, amp: amphibole, dol: dolomite.

3.1.3 Geologic structure

The Xiajinbao mining area located in the junction of the tectonic belt. The fault structures are very well developed. Based on the strike, the fault in the Xiajinbao mining area can be classified into two types: NE-SW trending fault structure and W-E trending structure (Fig. 5).

The F2 fault has a strike and dip of NE and 40° to 52°NW, respectively. It cross cut the granite porphyry and goes into Archean gneiss in the north of the Xiajinbao mining area. The dip direction of F2 fault is similar to the ore which suggest the F2 fault could be contributed to the mineralization. The largest-scale fault (F4) having a strike and dip of 40° to 70°NE and 40° to 65°SE, respectively. The F4 is located in the east of the F2 fault and generated a 5 to 20m wide breccia zone in the Xiajinbao mining area. The dip direction of F4 fault is opposite to the ore. The formation of the F4 fault is thought to be later than the emplacement of granite porphyry and there is no mineralization in the fault zone.

The E-W trending faults develop in the east portion of Xiajinbao mining area. The normal fault set F11 develop between the dolomite and sandstone and between the sandstone and granite porphyry. The strike and dip of the F11 are E-W and 70 to 85°S, respectively.

3.2 Geologic characteristics of ore deposit

3.2.1 Mode occurrence of ore deposit

The orebodies of the Xiajinbao deposit occur mainly in the granite porphyry (Fig. 5). The orebodies occur in an area of 800 m by 300 m in the granite porphyry. The orebodies are composed of aggregates of a large number of veins and veinlets having widths from 5 cm to 1 mm. These veins and veinlets are divided into three types: pyrite quartz veins, pyrite-chalcopyrite quartz veins and sphalerite-galena quartz veins (Figs. 11a, d and g). The general strikes and dips of these veins are 30 to 40° NE-SW and 40 to 80° NW, respectively. In the deep part of the orebodies, pyrite-chalcopyrite quartz veins are dominant. On the other hand, in the shallow part of the orebodies, sphalerite-galena quartz veins are dominant. The thickness of the bonanza that is composed of aggregates of these veins ranges from 1 to 15 m. The average Au grade of the Xiajinbao deposit is 1.9 g/t. The average Au grade of the bonanza is 7.5 g/t. The part having the highest Au grade (222 ppm) is in a sphalerite-galena quartz vein-dominant area in the shallow part of the Xiajinbao deposit. Diorite dikes are also present near the Au-rich part in the underground workings of the Xiajinbao deposit (Fig. 7).

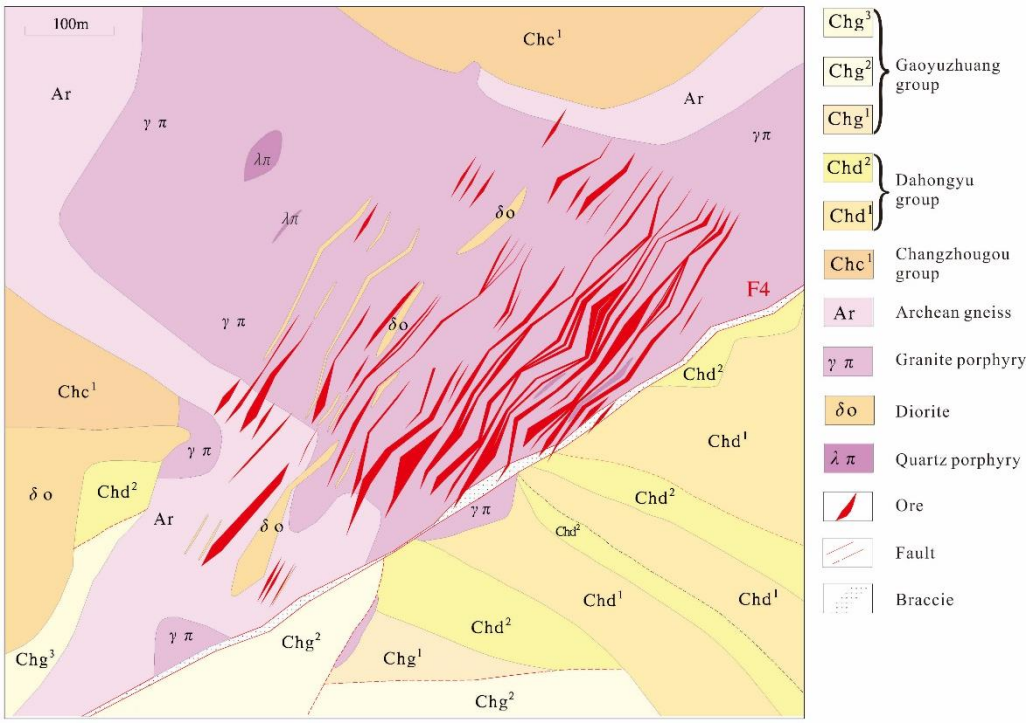

Fig. 9 Projection geologic map of 100m deep of the Xiajinbao mining area. The assay data of gold were collect from the underground tunnel and drill core. Modify from Hebei Bureau of geology and mineral resources exploration (1992).

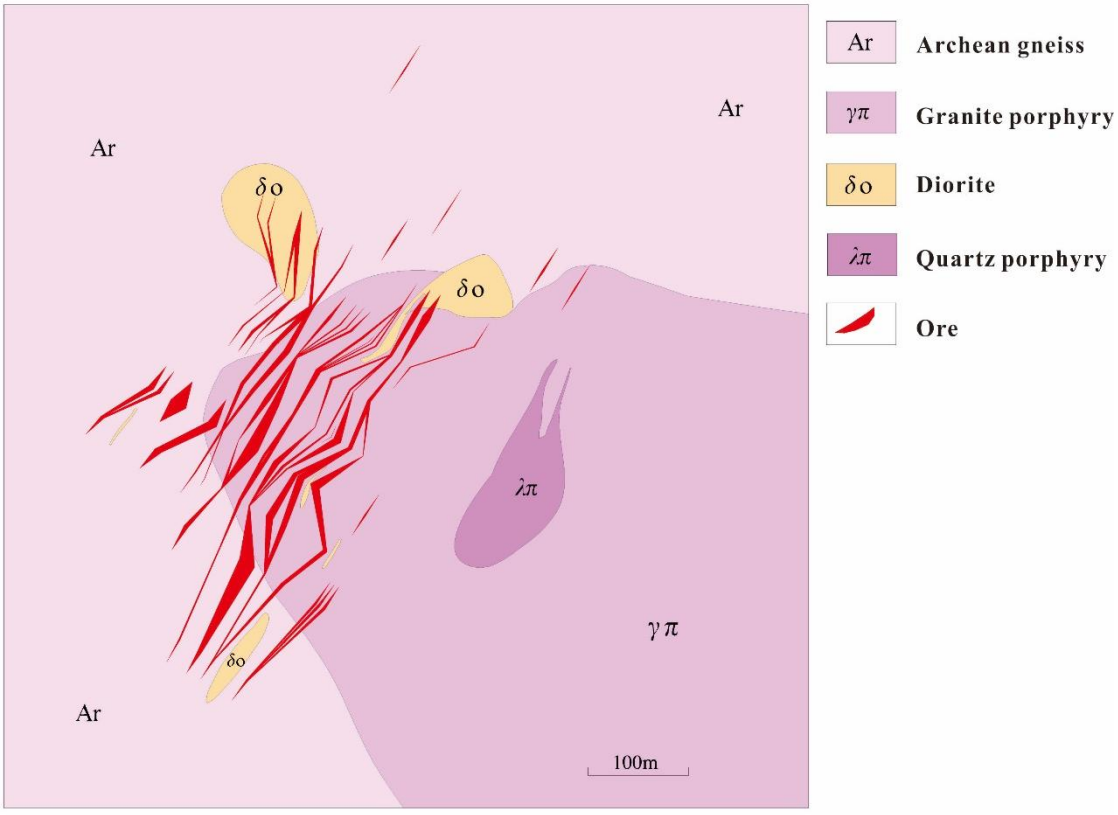

Fig. 10 Projection geologic map of 400m deep of the Xiajinbao mining area. Modify from Hebei Bureau of geology and mineral resources exploration (1992).

In the deeper portion (Fig. 10), the distribution of the ore goes to west part of the granite porphyry and the internal to external contact zone. In the contact zone between granite porphyry and Archean gneiss, intensive the diorite dikes are also distributed. The distribution of diorite dikes is in accordance with the distribution of areas having high Au contents. It seems the diorite dike and the gold mineralization has certain spatial relationship.

3.2.2 Mineral assemblage and mineralization stage

Pyrite quartz veins, pyrite-chalcopyrite quartz veins and sphalerite-galena quartz veins were observed in the Xiajinbao deposit (Figs. 11a, d, g). The sphalerite-galena quartz veins contain a large amount of gold. The pyrite quartz veins are cut by the pyrite-chalcopyrite quartz veins. The sphalerite-galena quartz veins cut the pyrite quartz veins and pyrite-chalcopyrite quartz veins (Fig. 11d). Based on these cross-cutting relations, the sequence of

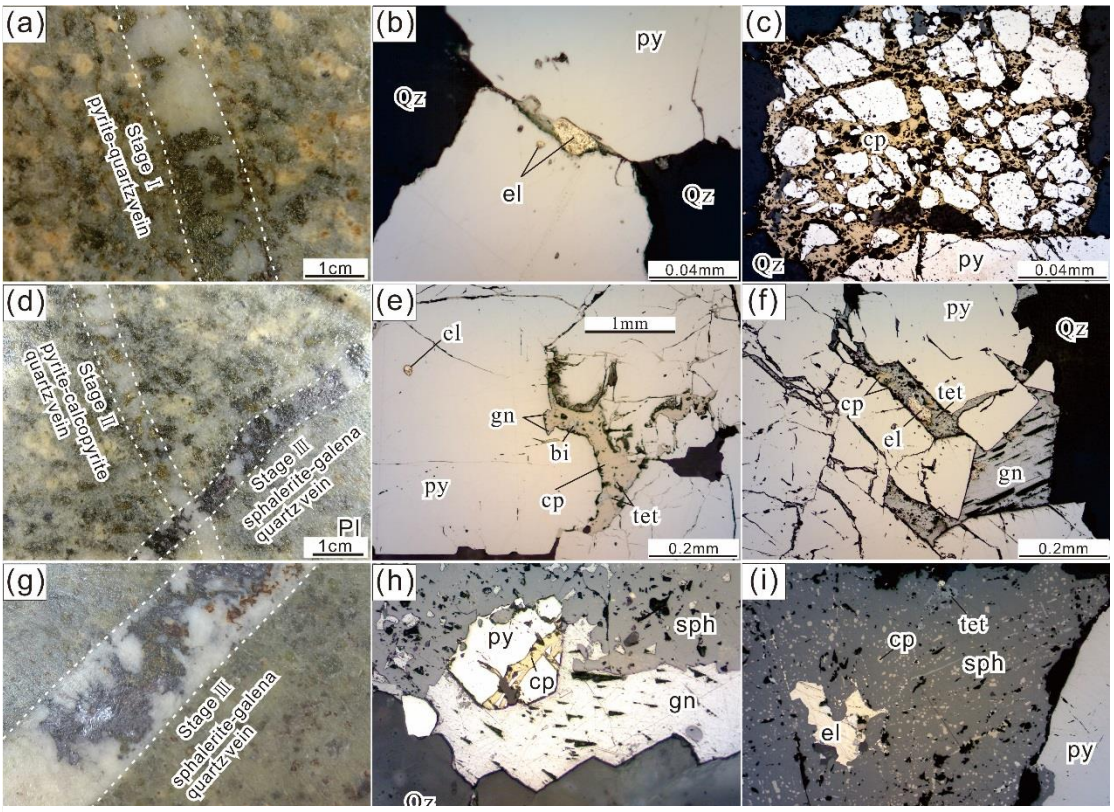

Fig. 11 Pictures of pyrite quartz vein, pyrite-chalcopyrite quartz vein and sphalerite-galena quartz vein and photomicrographs of ore minerals in these vein. (a) Pyrite quartz vein. (b) Electrum between pyrite crystals. (c) Network of chalcopyrite in pyrite crystals in pyrite quartz vein. (d) Mode occurrence showing pyrite-chalcopyrite quartz vein that is cut by sphalerite-galena quartz vein. (e) Galena-chalcopyrite-tetrahedrite-native bismuth veinlet in pyrite crystal of pyrite-chalcopyrite quartz vein. Electrum is also present in pyrite. (f) Galena, tetrahedrite and electrum veinlet in pyrite crystal in pyrite-chalcopyrite quartz vein. (g) Sphalerite-galena quartz vein. (h) Photomicrograph showing mode of occurrence of chalcopyrite veinlet cutting pyrite crystal, sphalerite and galena crystals in sphalerite-galena quartz vein. (i) Photomicrograph showing mode of occurrence of electrum in spalerite-galena quartz vein. Abbreviations: py: pyrite; el: electrum; cp: chalcopyrite; sph: sphalerite; gn: galena; tet: tetrahedrite; bi: native bismuth.

mineralization is thought to be in the order from pyrite quartz veins (Stage I), pyrite-chalcopyrite quartz veins (Stage II) and sphalerite-galena quartz veins (Stage III). The mineral assemblages of these veins are summarized in Fig. 12 (Li et al., 2018).

Pyrite quartz veins are composed of large amounts of quartz and pyrite with small amounts of chalcopyrite and electrum (Fig. 11a). The pyrite crystals mostly have a euhedral shape with diameters 0.1 to 2 mm (Fig. 11b). The chalcopyrite with an anhedral shape cuts the euhedral pyrite (Fig. 11c). The electrum in this stage was observed in interstices between quartz and pyrite crystals (Fig. 11b).

Pyrite-chalcopyrite quartz veins are composed of large amounts of quartz, pyrite and chalcopyrite. Electrum is also present in pyrite crystals as isolated grains (Fig. 11e). Small amounts of chalcopyrite, galena, tetrahedrite, native bismuth and electrum occur in fractures of pyrite (Fig. 11e). The same mineral assemblage as that in the fractures of pyrite is also observed in sphalerite-galena quartz vein. Based on this fact, this mineral assemblage is thought to have been formed by mineralization in Stage Ⅲ.

Sphalerite-galena quartz veins are composed of large amounts of quartz, sphalerite and galena, small amounts of pyrite and chalcopyrite, and trace amounts of native bismuth, tetrahedrite and electrum (Figs. 11h and 11i). Two types of electrum were observed in this stage. One type of electrum occurs with galena, chalcopyrite, native bismuth and tetrahedrite as veinlets in pyrite crystals (Fig. 11f), and the other type of electrum occurs as anhedral isolated grains in sphalerite crystals. The electrum of the second type has a lighter yellow color than that of the first type.

3.2.3 Chemical composition of ore minerals

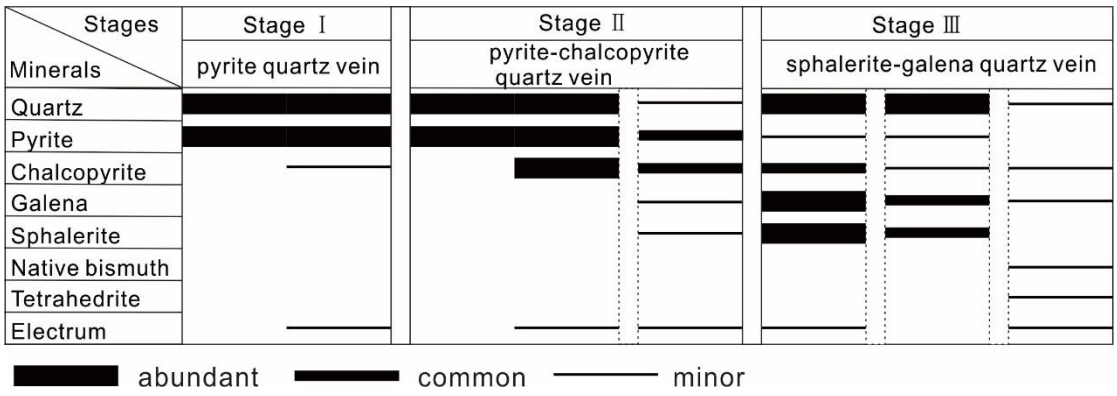

Fig. 12 Mineral assemblage and paragenetic sequence of the Xiajinbao deposit.

3.3 Geochemical characteristics of igneous rocks

3.3.1 Alteration

Wall rock alteration of the Xiajinbao deposit is characterized by quartz-illite-pyrite alteration with the subordinate presence of fluorite and carbonate minerals. Quartz-illite-pyrite alteration prevails from deep to shallow parts of the orebody of the Xiajinbao deposit. The amount of illite in altered rocks of sphalerite-galena quartz veins is larger than the amount of illite in altered rocks of pyrite quartz veins and pyrite-chalcopyrite quartz veins. The color of the altered granite porphyry near the sphalerite-galena quartz veins changes from reddish to green with increase in the degree of alteration. This green color was caused by the illite alteration. Silicification was also observed along these veins.

To confirm the degrees of alteration for granite porphyry, diorite and quartz porphyry dikes, the alteration index (AI) and chlorite-carbonate-pyrite index (CCPI) (Ishikawa et al., 1976; Large et al., 2001) were calculated. The Ishikawa alteration index (AI) and the chlorite-carbonate-pyrite index (CCPI) are two indicators for the type and degree of alteration of volcanic rocks. AI index was defined by Ishikawa et al. (1976) to quantify the intensity of sericite and chlorite alteration that occurs in the footwall volcanics proximal to Kuroko deposits which is mainly indicated by mobile elements such as K, Na, and Ca. These elements are easy to be transferred during the breakdown of sodic plagioclase and volcanic glass and their replacement by other alteration minerals. CCPI index is designed to measure the increase in MgO and FeO associated with the Mg-Fe chlorite development, which commonly replaces albite, K feldspar, or sericite in the volcanic rock, leading to a loss of Na_2O and K_2O.

In the alteration box (Fig. 13), AI and CCPI values of granite porphyry range from 52.7 to 66.1 and 23.4 to 26.9, respectively. Some of the granite porphyry has slightly higher AI values caused by alteration. However, most of the granite porphyry is plotted in the least altered box. AI and CCPI values of the diorite dike in the outcrop are 39.2 and 72.3, respectively. AI and CCPI values of the diorite dike underground are 39.4 and 58.5, respectively. AI and CCPI values of the quartz porphyry dike are 53.4 and 10.4, respectively.

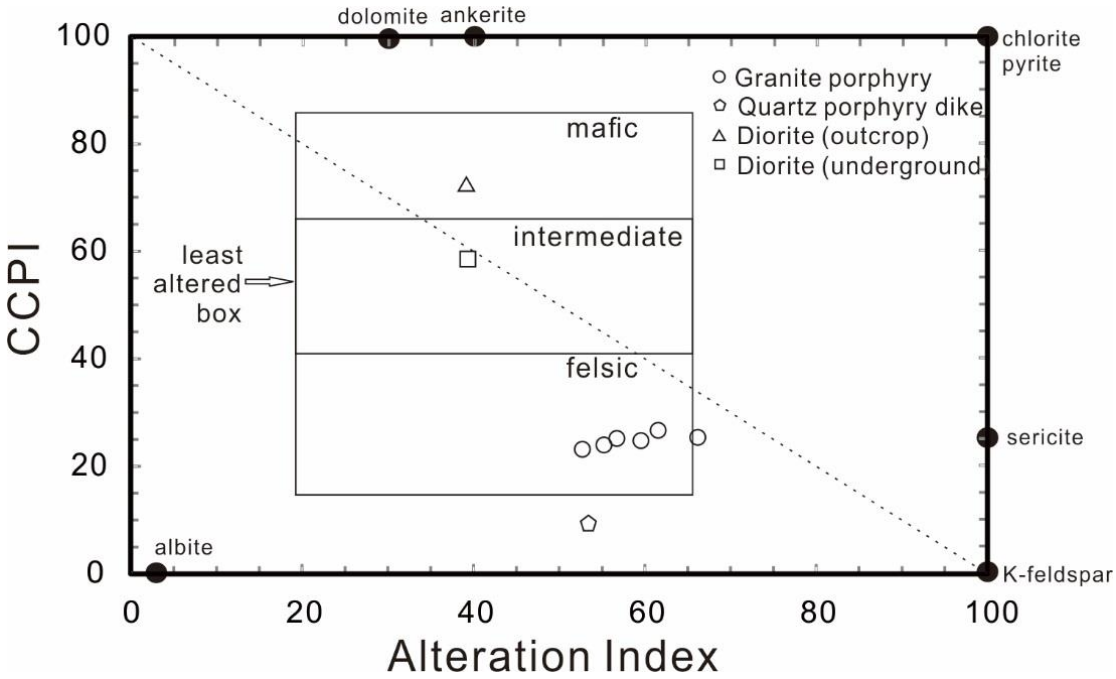

Fig. 13 Alteration box of the igneous rocks in the Xiajinbao deposit. The AI and CCPI values are shown in Table 1.

The CCPI value of the quartz porphyry dike is plotted outside the box of felsic rocks because of the quartz porphyry dike is characterized by low T-Fe_2O_3 and MgO contents originally (Fig. 13). The granite porphyry is mostly plotted in the least altered box, while the AI values indicate the sericite alteration trend in the granite porphyry. This fact is in accordance with the mineral assemblage observed under the microscope, which indicates that the dominant alteration in Xiajinbao deposit is illitization (hydromuscovite or sericite).

Based on the mineralogical characteristics, diorite dikes, granite porphyry and quartz porphyry dikes contain some clay minerals. The granite porphyry and quartz porphyry dikes could be classified as weakly altered rocks.

3.3.2 Chemical composition

Chemical compositions of igneous rocks of the Xiajinbao deposit are shown in Table 1. The SiO_2 and TiO_2 contents of granite porphyry are around 70 wt% and 0.2 wt%, respectively (Fig. 14). The Al_2O_3 contents of granite porphyry range from 13.9 to 14.3 wt%. The T-Fe_2O_3 contents of granite porphyry range from 1.9 to 2.5 wt%. The FeO contents of granite porphyry range from 1.1 to 1.7 wt%. The MgO contents of granite porphyry are around 0.5 wt%. The Na_2O and K_2O contents of granite porphyry range from 2.3 to 2.9 wt% and 4.6 to 6.1 wt%, respectively.

The SiO_2 and Al_2O_3 contents of diorite dikes are 49.1 to 51.1 wt% and 13.7 to 16.3 wt%, respectively (Fig. 14). The TiO_2 content of diorite dikes ranges from 1.0 to 3.1 wt%. The T-Fe_2O_3 content of diorite dikes is 7.3 to 11.5 wt%. The Na_2O and K_2O contents of diorite dikes are 3.3 to 4.1 wt% and 2.4 to 2.9wt%, respectively.

The SiO_2 and Al_2O_3 contents of quartz porphyry dikes are 75.8 wt% and 13.1 wt%, respectively. The T-Fe_2O_3 content of quartz porphyry dikes is 0.8 wt%. The Na_2O and K_2O contents of quartz porphyry dike are 2.4 wt% and 4.4 wt%, respectively.

From the Harker diagram shown in Fig. 14, concentrations of some mobile elements are thought to have changed, even though the studied samples are considered to be weakly altered. Most of the granite porphyry samples plot very close to each other. For the weakly altered one, the K_2O content tends to be increased while Na_2O and CaO tend to be slightly decreased. In general, the granite porphyry in the Xiajinbao deposit has low TiO_2, CaO, Na_2O, and P_2O_5 values. These features are similar to the S-type granitic rock presented by Chappell and White (1992). Another classification for granitic rock is reported by Ishihara (1977), which is the ilmenite-series (corresponding to S-type) and magnetite series (corresponding to I-type). The ilmenite-series or S-type granitic rocks represent a reduced formation environment while the magnetite-series or I-type series represent an oxidized environment. In the Xiajinbao granite porphyry, the Fe content is much higher than the Mg content. The FeO/Fe_2O_3 ratio of the granite porphyry range from 0.33 to 0.59. The Fe/(Fe+Mg) ratio of granite porphyry range from 0.80 to 0.84. These features are close to the ilmenite-series granitic rocks.

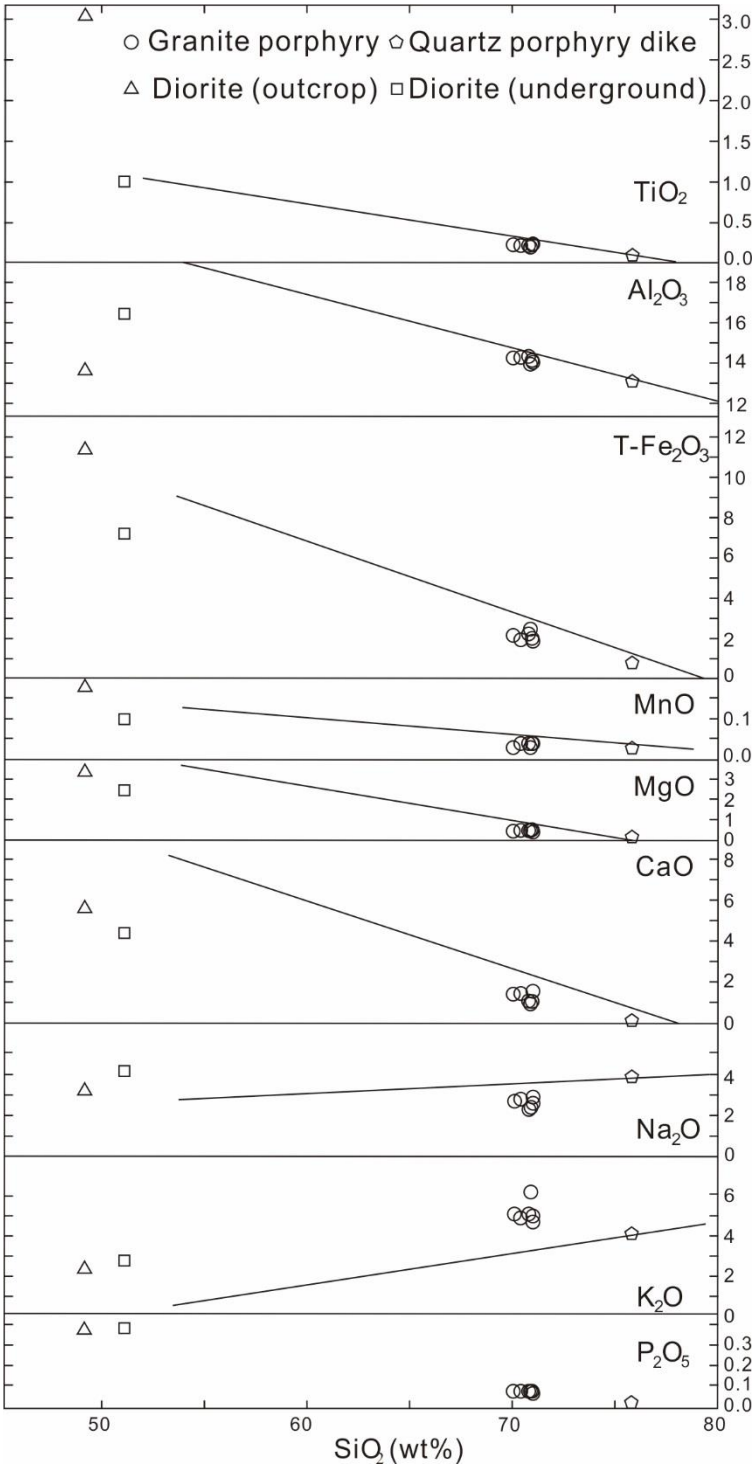

Fig. 14 Harker diagrams of igneous rocks in the Xiajinbao mining area. Lines correspond to the average chemical composition of granitoids in Japan.

Table 1 Chemical composition of igneous rocks in the Xiajinbao mining area.

Sample	Z153	Z144-2	Z176-2	Z190-1	Z188	Z175-3	132-2	Z45	132-1
	Granite porphyry						Quartz porphyry dike	Diorite dike (underground)	Diorite dike (outcrop)
wt%									
SiO_2	71.0	70.4	70.1	71.0	70.8	70.9	75.8	51.1	49.1
TiO_2	0.2	0.2	0.2	0.2	0.2	0.2	0.1	1.0	3.1
Al_2O_3	14.1	14.3	14.3	14.1	14.3	13.9	13.1	16.3	13.7
T-Fe_2O_3	1.9	1.9	2.2	2.0	2.2	2.5	0.8	7.3	11.5
FeO	1.1	1.3	1.2	1.1	1.5	1.7	-	-	-
MnO	0.04	0.04	0.03	0.04	0.04	0.03	0.03	0.14	0.16
MgO	0.4	0.5	0.5	0.5	0.5	0.5	0.2	2.6	3.4
CaO	1.6	1.4	1.4	1.1	1.1	0.9	0.1	4.2	5.7
Na_2O	2.9	2.8	2.7	2.6	2.3	2.4	3.9	4.1	3.3
K_2O	4.6	4.8	5.0	4.9	5.0	6.1	4.4	2.9	2.4
P_2O_5	0.07	0.08	0.08	0.08	0.08	0.08	0.01	0.42	0.38
LOI	2.2	2.4	2.5	2.3	2.5	2.5	1.2	9.8	6.4
Total	98.9	98.9	98.9	98.9	99.0	100.0	99.6	99.9	99.4
ppm									
Zr	132	198	154	202	152	149	61	152	178
AI	52.7	55.2	56.7	59.5	61.5	66.1	53.4	39.4	39.2
CCPI	23.4	24.2	25.4	25.0	26.9	25.6	10.4	58.5	72.3
ASI	1.12	1.15	1.15	1.22	1.28	1.13	1.15	0.93	0.75

Abbreviations: AI=100(K_2O+MgO)/(K_2O+MgO+Na_2O+CaO); CCPI=100(MgO+FeO)/(MgO+FeO+Na_2O+K_2O); ASI=Al_2O_3/(CaO+Na_2O+K_2O)

Alteration index (AI): Ishikawa et al. (1976), Chlorite-carbonate-pyrite index (CCPI): Large et al. (2001).

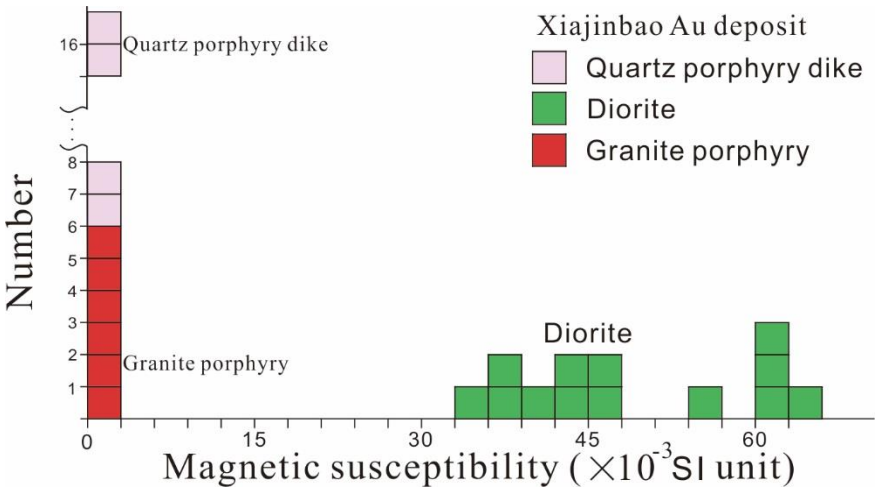

Fig. 15 Magnetic susceptibility of igneous rocks in the Xiajinbao deposit.

The values of the aluminum saturation index (ASI) is one of the indicators for metaluminous and peraluminous rocks. The ASI for granite porphyry and quartz porphyry dikes were examined. The ASI value of granite porphyry ranges from 1.12 to 1.28. The ASI value of quartz porphyry is 1.15, which is within the range of the ASI value of the granite porphyry. In addition, the magnetic susceptibility of granite porphyry, quartz porphyry, and diorite were measured in the field (Fig. 15). The granite porphyry and quartz porphyry dikes have a low magnetic susceptibility smaller than 0.1×10^{-3} SI unit, while the diorite has a magnetic susceptibility from 15 to 60×10^{-3} SI unit. The high ASI values, low magnetic susceptibility and presence of ilmenite in the granite porphyry and quartz porphyry dikes suggest that granite porphyry and quartz porphyry dikes in the Xiajinbao deposit belong to ilmenite-series granitic rocks (Li et al., 2018). The higher magnetic susceptibility and the occurrence of magnetite in the diorite dikes suggest that the diorite dikes were formed by oxidized magma.

Based on the chemical composition, CIPW norm mineral calculation was accomplished after the calculation steps of Johannsen (1931). The normative minerals are quartz, plagioclase, orthoclase, corundum, hypersthene, ilmenite, apatite, hematite and zircon. Normative corundum, as a key CIPW mineral, shows different ranges of lower than 1 wt% in I-type and higher than 1 wt% in S-type granitic rocks. In the Xiajinbao granite porphyry, the calculated normative corundum ranges from 1.5 to 2.0 wt%.

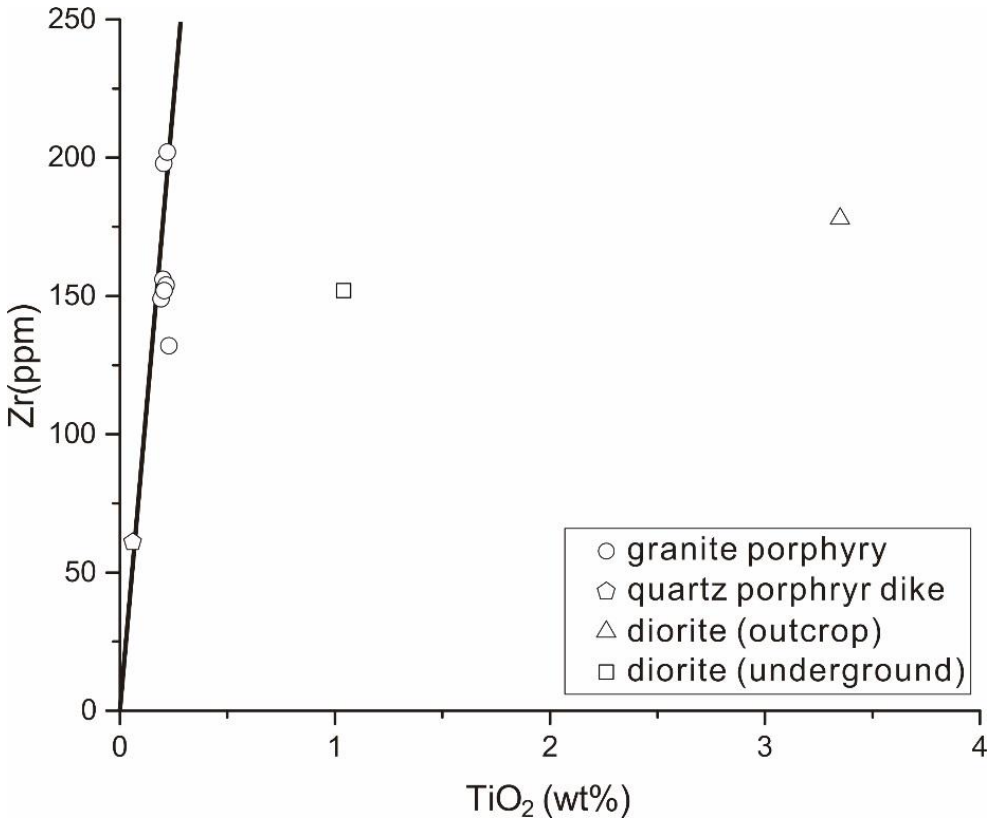

Fig. 16 TiO_2-Zr diagram of the igneous rocks in the Xiajinbao deposit.

The Zr/TiO_2 ratios of igneous rocks in the Xiajinbao mining area are shown in Fig. 11. The Zr/TiO_2 ratios of granite porphyry and quartz porphyry dikes are both around 770 (Fig. 16). On the other hand, the Zr/TiO_2 ratios of diorite dikes in the underground and outcrop are approximately 150 and 60, respectively, and they are different from the ratios of granite porphyry and quartz porphyry dikes (Li et al. 2018). These ratios indicate that the characteristics of magma of granite porphyry and quartz porphyry dikes are similar. On the other hand, they are different from the characteristics of magma of diorite dikes. The igneous activities of the Xiajinbao mining area are thought to be bimodal igneous activities.

3.3.3 Trace elements

The Chondrite-normalized rare earth element patterns are shown in Fig. 18 and Fig. 17, respectively. The Chondrite-normalized rare earth element patterns are similar to those patterns for the upper crust. The trace elements of granite porphyry were characterized by high concentrations of incompatible elements such as the rare earth elements (REE) and large-ion lithophile elements (LILE). All the samples show similar fractionated REE patterns characterized by significant LREE enrichment with δEu values of 0.6 to 0.7. There is a very weak Eu anomaly. Drake (1975) suggested that there is an inverse relation between δEu and fo_2. The total REE contents in the granite porphyry are ranged from 146.2 to 163.8 ppm. The LREE/HREE value ranged from 14.0 to 18.3, which suggest that the LREE is much higher than the HREE and there is a differentiation between the rare earth elements.

Table 2 Trace elements of granite porphyry in the Xiajinbao deposit.

Elements (ppm)	Z144-2	Z153	Z176-2	Z188	Z190-1
Rb	136.0	116.0	104.0	119.0	110.0
Ba	1083.0	1132.0	980.0	1001.0	977.0
Th	11.0	10.5	8.8	9.3	9.3
U	1.8	3.0	2.6	2.3	3.1
K	395.4	378.0	411.2	412.0	407.0
Ta	0.8	0.8	0.7	0.7	0.8
Nb	13.0	11.4	10.9	11.3	11.5
La	39.9	45.2	37.6	42.4	38.0
Ce	71.1	76.6	65.6	73.7	67.0
Sr	215.0	290.0	211.0	160.0	176.0
Nd	27.1	27.2	23.9	27.0	24.8
P	3.4	3.2	3.6	3.6	3.4
Zr	198.0	132.0	154.0	152.0	202.0
Hf	5.9	4.2	4.9	5.0	6.2
Sm	4.3	3.9	3.5	3.8	3.5
Ti	12.3	13.7	12.9	12.4	13.3
Y	15.1	12.0	10.7	11.2	11.0
Yb	1.8	1.4	1.3	1.3	1.3
Lu	0.3	0.2	0.2	0.2	0.2

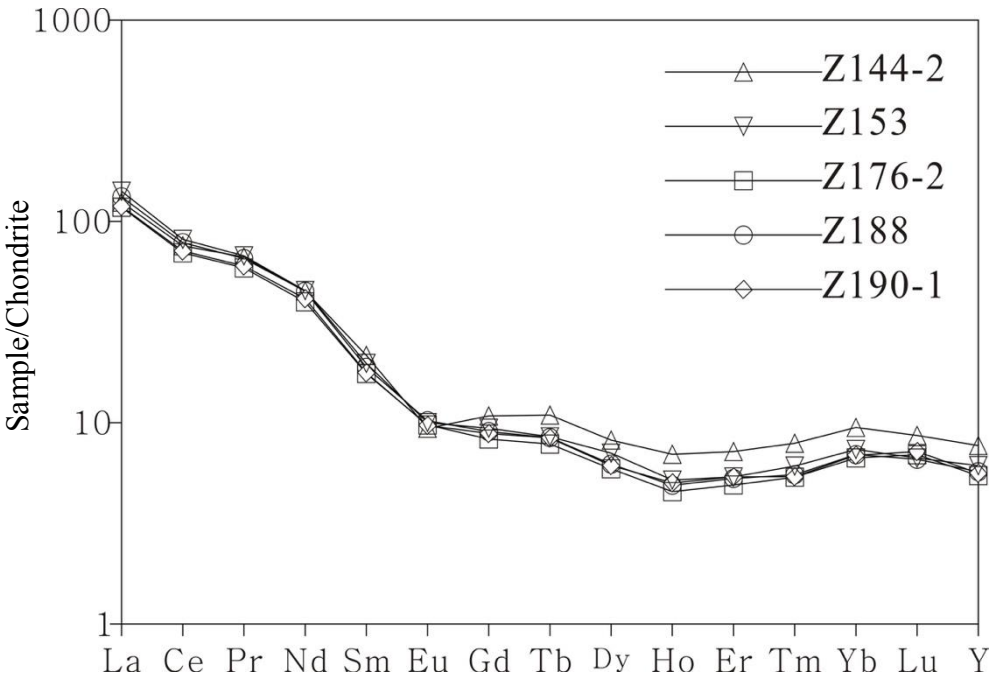

Fig. 17 Chondrite-normalized rare earth element patterns the granite porphyry in the Xiajinbao deposit .

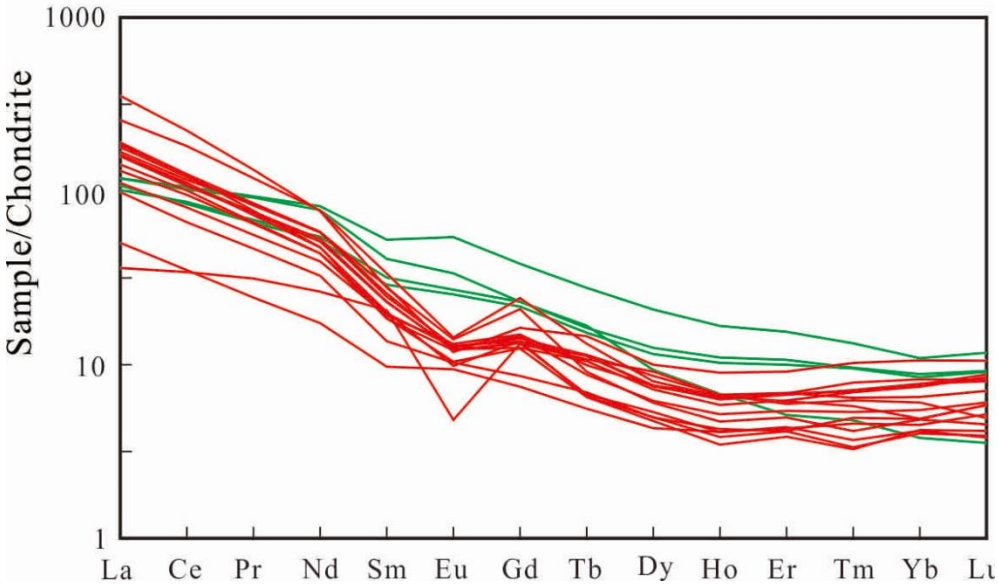

Fig. 18 Comparison of Chondrite-normalized rare earth element between granite porphyry and diorite in the Xiajinbao deposit. Reddish-grenite porphyry, green-diorite dike.

Table 3 Rare earth element of granite porphyry in the Xiajinbao deposit.

Elements (ppm)	Z144-2	Z153	Z176-2	Z188	Z190-1	Average
La	39.9	45.2	37.6	42.4	38.0	40.6
Ce	71.1	76.6	65.6	73.7	67.0	70.8
Pr	8.0	8.1	7.1	7.9	7.2	7.6
Nd	27.1	27.2	23.9	27.0	24.8	26.0
Sm	4.3	3.9	3.5	3.8	3.5	3.8
Eu	0.7	0.7	0.7	0.7	0.7	0.7
Gd	3.4	2.9	2.6	2.8	2.7	2.9
Tb	0.5	0.4	0.4	0.4	0.4	0.4
Dy	2.5	2.2	1.8	1.9	1.9	2.1
Ho	0.5	0.4	0.3	0.4	0.4	0.4
Er	1.5	1.1	1.0	1.1	1.1	1.2
Tm	0.3	0.2	0.2	0.2	0.2	0.2
Yb	1.8	1.4	1.3	1.3	1.3	1.4
Lu	0.3	0.2	0.2	0.2	0.2	0.2
Y	15.1	12.0	10.7	11.2	11.0	12.0
ΣREE	161.9	170.6	146.2	163.8	149.5	158.4
LREE	151.1	161.8	138.4	155.5	141.3	149.6
HREE	10.8	8.8	7.8	8.3	8.3	8.8
LREE/HREE	14.0	18.3	17.7	18.7	17.1	17.2
δEu	0.6	0.7	0.8	0.7	0.7	0.7
δCe	0.8	0.8	0.8	0.8	0.8	0.8
(La/Yb)N	13.2	19.2	17.6	19.1	17.2	17.2
(Ce/Yb)N	8.0	11.1	10.4	11.3	10.3	10.2
(La/Sm)N	5.8	7.2	6.7	7.0	6.7	6.7
(Gd/Yb)N	1.1	1.3	1.2	1.3	1.3	1.2

3.3.4 Age of igneous rocks

The age of the granite porphyry was determined by zircon U-Pb isotope geochronology method. Zircon was separated using conventional crushing, heavy liquid, and magnetic separation techniques and hand-picked under a binocular microscope. It was then mounted onto epoxy resin disks and polished to near half thickness in order to expose internal structures. Before the U–Pb dating, zircon internal textures were studied by the cathodoluminescence (CL) technique. Fracture and enclave-free grains and spots within grains were selected based on microscopy observation and cathodoluminescence images for analyses. A total of 15-30 spots on 10–30 zircon grains from each samples were analyzed. The age of each data were calculated by the ISOPLOT software (Ludwig, 2003).

The zircon in the granite porphyry has typical magmatic oscillatory zoning (Fig. 19). Most of the data are concordant, and yield $^{206}Pb/^{238}U$ weighted mean ages of 163.3 ± 0.9 Ma (Fig. 20).

Fig. 19 Cathodoluminescence image of zircon in the granite porphyry of the Xiajinbao deposit.

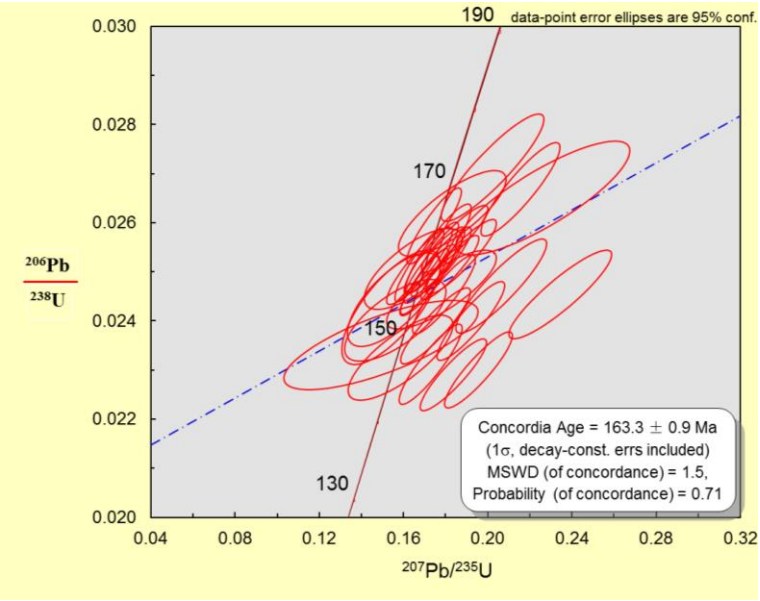

Fig. 20 Zircon U-Pb age of granite porphyry in the Xiajinbao deposit.

The age of the diorite dike in the Xiajinbao deposit was also analyzed. In the cathodoluminescence images, the zircon in the diorite dike also shows typical oscillatory zoning (Fig. 21). These zircons were thought to be magmatic zircons. However, some of the zircon in the diorite dike shows ellipse shape and having a light color halo in the outside margin of the zircon crystal. These zircons were thought to be effected by the latter stage hydrothermal alteration.

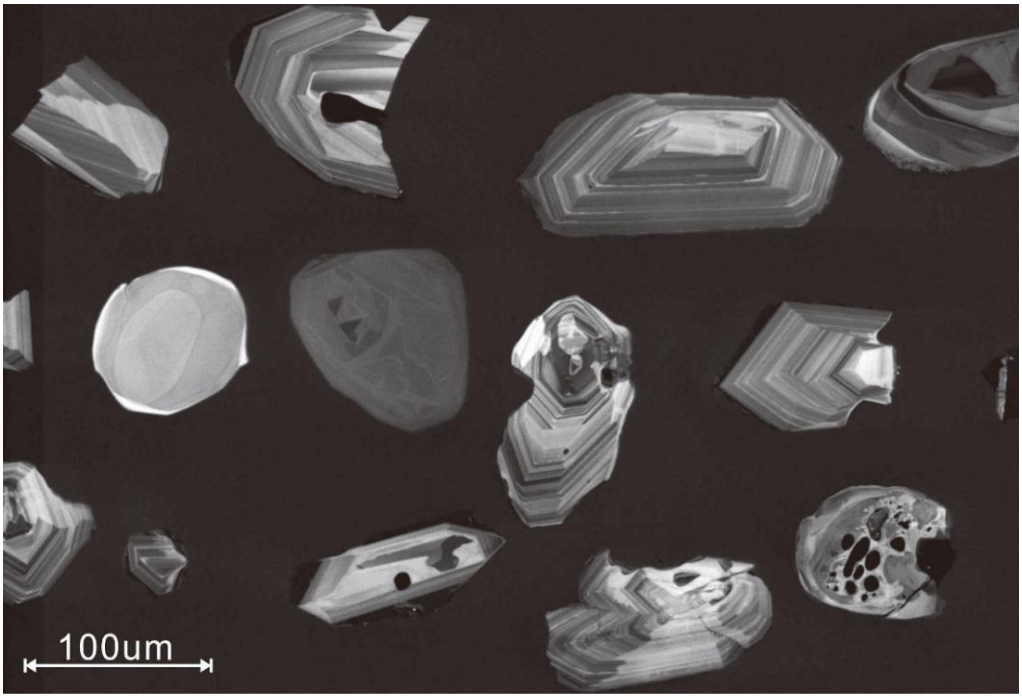

Fig. 21 Zircon U-Pb age of granite porphyry in the Xiajinbao deposit.

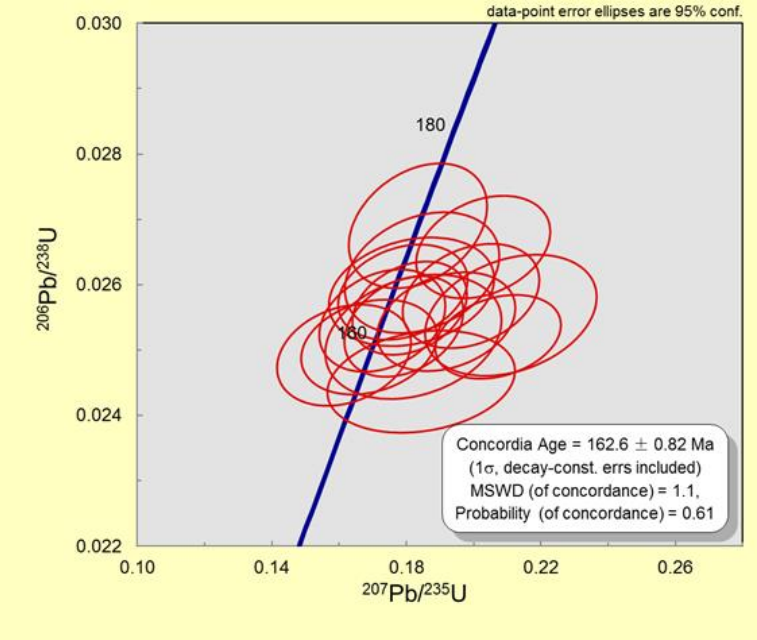

Fig. 22 Zircon U-Pb age of diorite dike in the Xiajinbao deposit.

The concordia age of the diorite dike in the Xiajinbao deposit was 162.6±0.82 Ma. This age data is similar to the age of the granite porphyry in the Xiajinbao deposit. Based on the age data, the emplacement of the igneous rocks in the Xiajinbao deposit might have formed in the same period.

3.4 Fluid inclusion studies

The fluid inclusions in quartz of pyrite quartz veins (Stage I), pyrite-chalcopyrite quartz veins (Stage II) and sphalerite-galena quartz veins (Stage III) were investigated (Table 3).

3.4.1 Petrography

Based on microscopic observation, most of the fluid inclusions have irregular shapes such as elliptical and strip shapes. The sizes of fluid inclusions ranged from 4 to 10 μm. All of the fluid inclusions in these samples were liquid-dominant vapor-liquid two-phase fluid inclusions (Fig. 23). All of the inclusions were homogenized into liquid phase when the fluid inclusions were heated. These facts suggest that there was no boiling during the mineralization.

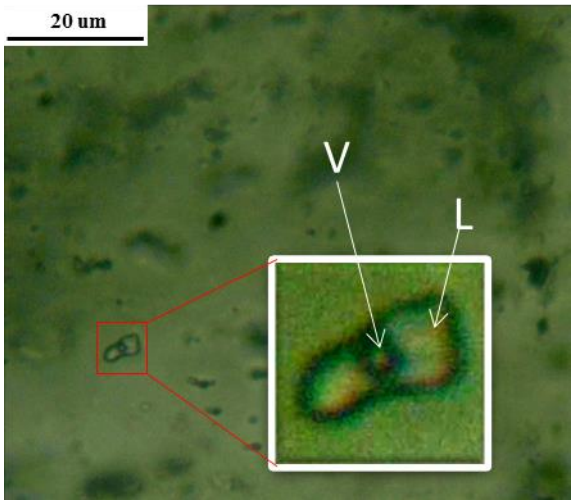

Fig. 23 Typical V-L two phase fluid inclusion in the quartz of Xiajinbao deposit.

3.4.2 Homogenization temperature and salinity

The homogenization temperatures of fluid inclusions in pyrite quartz veins range from 225 to 300°C with a mode of homogenization temperature at 265°C. Salinities of fluid inclusions in the pyrite quartz veins range from 6.0 to 11.4 wt% NaCl equivalent (Figs. 24 and 25). Homogenization temperatures of fluid inclusions in pyrite-chalcopyrite veins range from 215 to 290°C with a mode of homogenization temperature of 250°C. Salinities of the fluid inclusions in the pyrite-chalcopyrite quartz veins range from 6.2 to 12.6 wt% NaCl equivalent. Homogenization temperatures of fluid inclusions in sphalerite-galena quartz veins range from 175 to 260°C with a mode of homogenization temperature of 220°C. Salinities of the fluid inclusions in the sphalerite-galena quartz veins range from 9.1 to 13.8 wt% NaCl equivalent (Figs. 24 and 25). The homogenization temperatures of these veins decreased from pyrite quartz veins (Stage Ⅰ) to galena-sphalerite quartz veins (Stage Ⅲ) according to the progress of mineralization. On the other hand, salinities of fluid inclusions increased from Stage Ⅰ to Stage Ⅲ (Figs. 24 and 25) (Li et al., 2018)

The common mineral assemblage of alteration minerals of the Xiajinbao deposit is

quartz-illite-pyrite. Based on the presence of illite in the Xiajinbao deposit and stability of illite above 200°C (Henley et al., 1984), the formation temperature of the Xiajinbao deposit was estimated to be above 200°C. The temperature accords with the temperature of pyrite quartz veins, pyrite-chalcopyrite veins and sphalerite-galena quartz veins determined by the fluid inclusion study.

The salinity of fluid inclusions in gold-bearing sphalerite-galena quartz veins is higher than the salinities of fluid inclusions of the pyrite quartz veins and pyrite-chalcopyrite quartz veins (Fig. 25). Based on these data, there is a possibility that the contribution of magmatic components increased during the period of formation of the sphalerite-galena quartz veins.

Table 4 Microthermometric data for fluid inclusions in quartz of the pyrite quartz vein, pyrite-chalcopyrite quartz vein and sphalerite-galena quartz vein of the Xiajinbao deposit.

Sample	Type	mineral	Homogenization temperature (℃)	Final ice melting temperature (℃)	Salinity (NaCl wt% eq.)
Z31	pyrite quartz vein	quartz	273	-3.4	6.6
			224	-4.5	8.9
			236	-5.6	11.4
			301	-4.2	8.3
Z95	pyrite quartz vein	quartz	273	-4.7	9.4
			261	-3.8	7.4
			259	-4.1	8.1
			281	-3.5	6.8
			290	-4.3	8.5
			240	-3.1	5.9
			260	-3.6	7.0
			252	-4.8	9.6
			246	-5.2	10.5
			267	-4.6	9.1
Z47	pyrite-chalcopyrite quartz vein	quartz	223	-4.7	9.4
			247	-5.5	11.2
			253	-3.2	6.2
			286	-3.8	7.4
			269	-5.3	10.7
			216	-5.7	11.6
			246	-6.1	12.6
			219	-4.6	9.1
			231	-4.8	9.6
			259	-5.4	10.9
Z158	sphalerite-galena quartz vein	quartz	224	-5.2	10.5
			220	-5.4	10.9
			256	-5.6	11.4
			187	-4.6	9.1
			173	-4.8	9.6
			216	-5.4	10.9
			204	-6.2	12.8
			189	-5.3	10.7
			246	-6.6	13.8

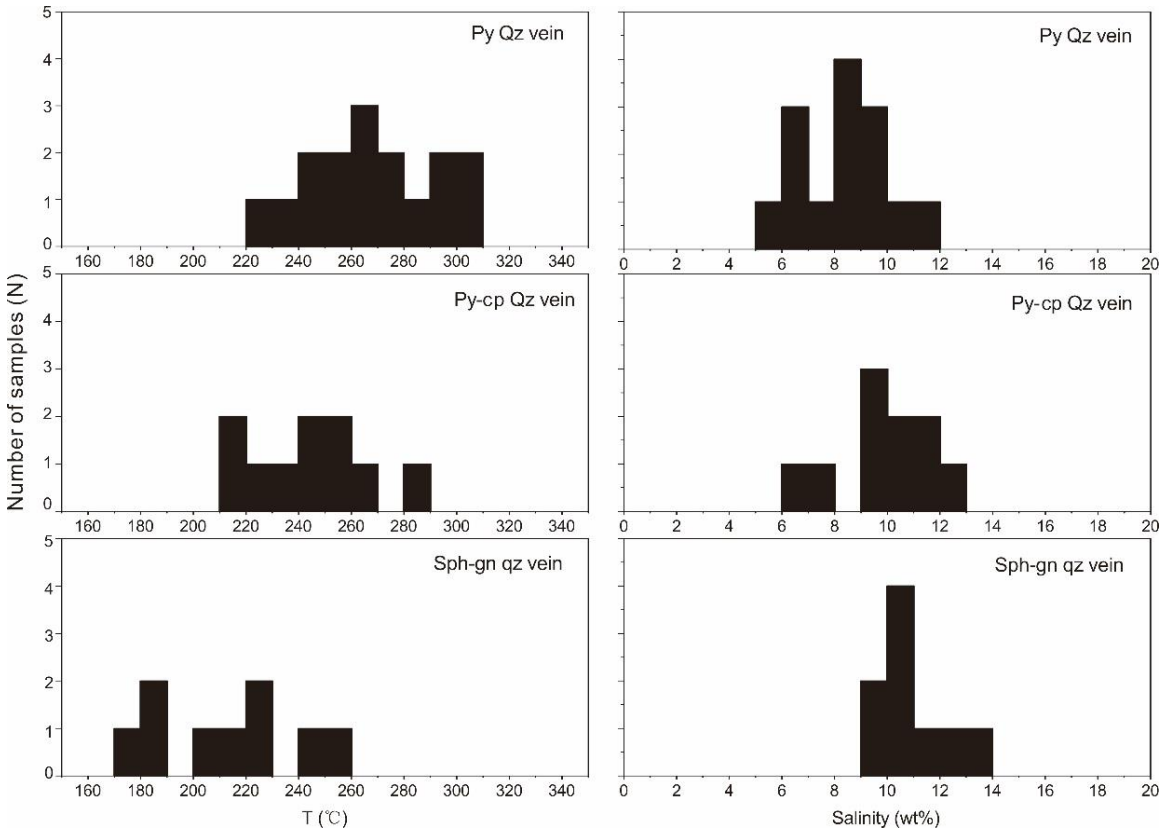

Fig. 24 Histogram of homogenization temperatures and salinities of pyrite quartz vein, pyrite-chalcopyrite quartz vein and sphalerite-galena quartz vein of the Xiajinbao deposit.

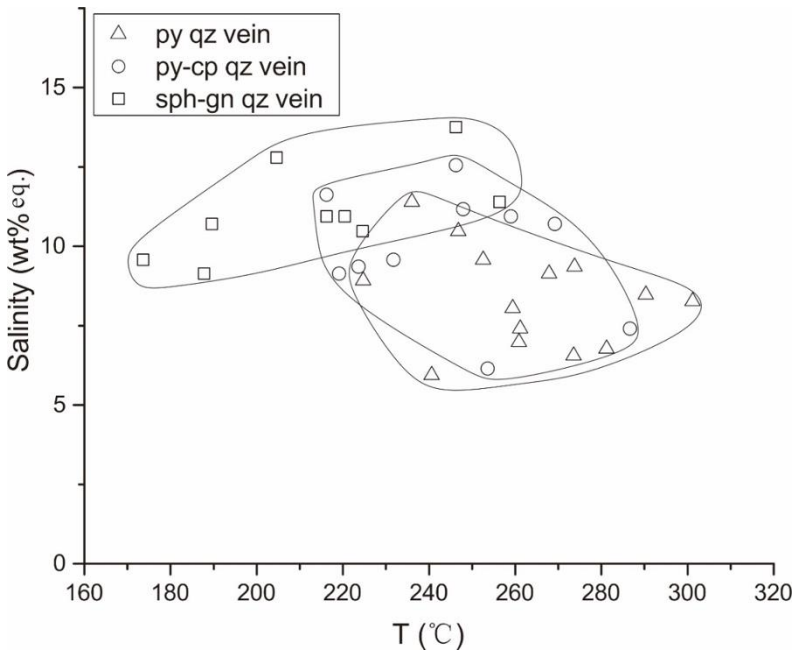

Fig. 25 Homogenization temperature-salinity diagram of fluid inclusions in pyrite quartz vein, pyrite-chalcopyrite quartz vein and sphalerite-galena quartz vein of the Xiajinbao deposit.

3.5 Oxygen, hydrogen, and sulfur isotope ratios of rocks and minerals

3.5.1 Oxygen and hydrogen isotope ratios

The $\delta^{18}O$ values of quartz from pyrite quartz veins, pyrite-chalcopyrite quartz veins and sphalerite-galena quartz veins range from +13.7 to +14.3‰, +13.6 to +13.7‰, and +14.5 to +16.7‰, respectively (Table 5; Fig. 26). The $\delta^{18}O$ value of hydrothermal solution forming gold-bearing quartz veins was estimated with the assumption of an isotopic equilibrium between quartz and H_2O (Matsuhisa et al., 1979) from the formation temperature and $\delta^{18}O$ value of quartz. Based on the homogenization temperature of fluid inclusion, $\delta^{18}O$ values of the hydrothermal solution in equilibrium with quartz in the pyrite quartz vein, pyrite-chalcopyrite quartz vein and sphalerite-galena quartz vein were estimated under temperatures of 265°C, 250°C and 220°C, respectively. The $\delta^{18}O$ values of the hydrothermal solution are +4.9 to +5.5‰, +4.2 to +4.3‰, and +3.3 to +5.5‰, respectively.

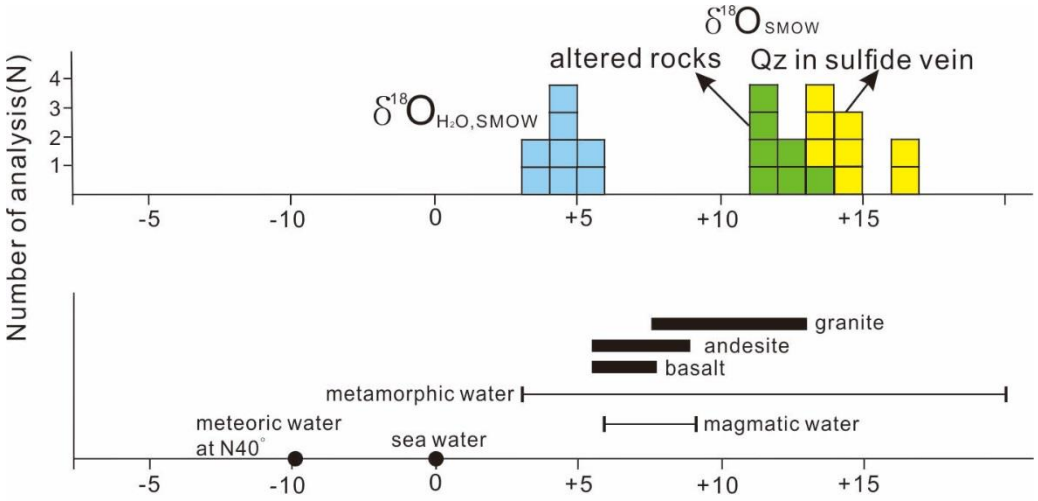

Fig. 26 Oxygen isotopic ratio of the Xiajinbao deposit.

The δD values of the hydrothermal solution were estimated with the assumption of an isotopic equilibrium between illite and H_2O from the fractionation factor between illite and H_2O (Sheppard and Gilg, 1996) and estimated formation temperature. The δD values of the hydrothermal solution in equilibrium with illite near pyrite quartz veins, pyrite-chalcopyrite quartz veins and sphalerite-galena quartz veins ranged from -39 to -42‰, -41 to -47‰ and -38 to -43‰, respectively. These $\delta^{18}O$ and δD values of the hydrothermal solution forming pyrite quartz veins and pyrite-chalcopyrite quartz veins are plotted near the area of felsic magmatic water and primary magmatic water (Fig. 27). The $\delta^{18}O$ values of sphalerite-galena quartz veins are similar to those of hydrothermal solution forming pyrite quartz veins and pyrite-chalcopyrite quartz veins and are close to the $\delta^{18}O$ value of magmatic water. These values suggest that the hydrothermal solution forming gold mineralization of the Xiajinbao

deposit was derived from magmatic water, regardless of whether the magmatic water was derived from oxidized magma or not.

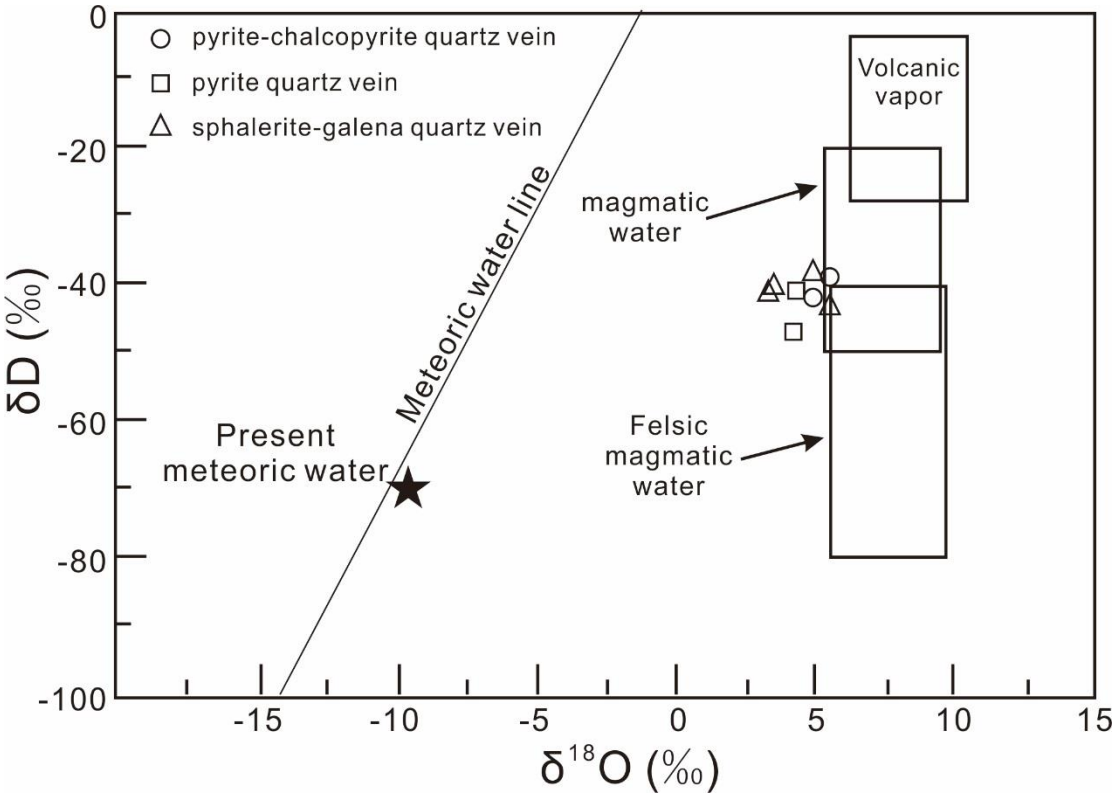

Fig. 27 Diagram showing calculated hydrogen and oxygen isotopic values of hydrothermal solution associated with formation of pyrite quartz vein, pyrite-chalcopyrite quartz vein and sphalerite-galena quartz vein of the Xiajinbao deposit. Meteoric water line (Craig, 1961), primary magmatic water (Taylor, 1992), felsic magmatic water (Taylor, 1979), volcanic vapor along subduction zone (Giggenbach, 1992).

The initial water related to the formation of pyrite quartz veins, pyrite-chalcopyrite quartz veins and sphalerite-galena quartz veins of the Xiajinbao deposit was also estimated on the basis of the final $\delta^{18}O$ values of altered rocks after oxygen isotopic exchange as a result of water and rock interaction (Taylor, 1971). The $\delta^{18}O$ values of altered rocks close to pyrite quartz veins, pyrite-chalcopyrite quartz veins and sphalerite-galena quartz veins range from +11.8 to +13.1‰, +11.3 to +11.4‰ and +11.4 to +12.1‰, respectively (Table 5). These values are similar. Assuming water-rock interactions of felsic igneous rocks having an initial $\delta^{18}O$ value of +8‰ with magmatic water, meteoric water and seawater, the final $\delta^{18}O$ value of rock after water-rock interaction can be estimated by the following equation (Taylor, 1971):

$$\delta^{18}O_f^r = \frac{(\delta^{18}O_i^r + (\delta^{18}O_i^w + 1000 \ln \alpha_{r\text{-}w})\, W/R}{1 + W/R},$$

where W/R is the water/rock ratio expressed as proportion of oxygen atoms, r and w refer to rock and water, respectively, i and f refer to the initial state and the final state, respectively, and 1000 $\ln\alpha_{r\text{-}w}$ is the fractionation factor between rock and H_2O (Matsuhisa et al., 1979).

Based on a comparison of oxygen isotope ratios of whole rock and minerals consisting of plutonic rocks, the oxygen isotope ratio of whole rock is similar to that of plagioclase with 30% An. Therefore, the fractionation factor between whole rock and water can be substituted by the fractionation factor between plagioclase (30% An) and H_2O (O'Neil and Taylor, 1967). In the case of water-rock interactions between felsic igneous rocks and seawater (Fig. 28) or meteoric water (Fig. 28) of temperatures from 200°C to 300°C, the $\delta^{18}O$ values of altered rock of those veins should be around +9 ‰ for seawater and -1 ‰ for meteoric water. These values are lower than the $\delta^{18}O$ values of altered rocks of the Xiajinbao deposit. On the other hand, in the case of water-rock interaction between felsic igneous rocks and magmatic water, the $\delta^{18}O$ values of final rock are estimated to be from +11.5 to +12.5‰. The estimated $\delta^{18}O$ values are similar to the $\delta^{18}O$ values of altered rocks of the Xiajinbao deposit. The calculations suggest that the alterations of the Xiajinbao deposit were formed by interaction between magmatic water and felsic rock under a water-dominant condition at temperatures from 200°C to 300°C (Fig. 28).

Table 5 Hydrogen isotopic ratios of illite, oxygen isotopic ratios of quartz and whole rock of the Xiajinbao deposit.

Sample	Depth	Type of vein	$\delta D_{illite,SMOW}$	$\delta^{18}O_{quartz,SMOW}$	$\delta D_{H2O,SMOW}$	$\delta^{18}O_{H2O,SMOW}$	$\delta^{18}O_{rock,SMOW}$
(‰)	(m)						
Z49	373.5	py-qz	-64	+14.3	-39	+5.5	+13.1
Z61	462.7	py-qz	-67	+13.7	-42	+4.9	+11.8
Z46	360.2	py-cp qz	-72	+13.6	-47	+4.2	+11.4
Z51	402.0	py-cp qz	-66	+13.7	-41	+4.3	+11.3
Z09	108.8	sph-gn qz	-65	+14.7	-40	+3.5	+12.1
Z15	164.0	sph-gn qz	-66	+14.5	-41	+3.3	+12.5
Z27	210.8	sph-gn qz	-68	+16.7	-43	+5.5	
Z71	531.5	sph-gn qz	-63	+16.1	-38	+4.9	+11.4

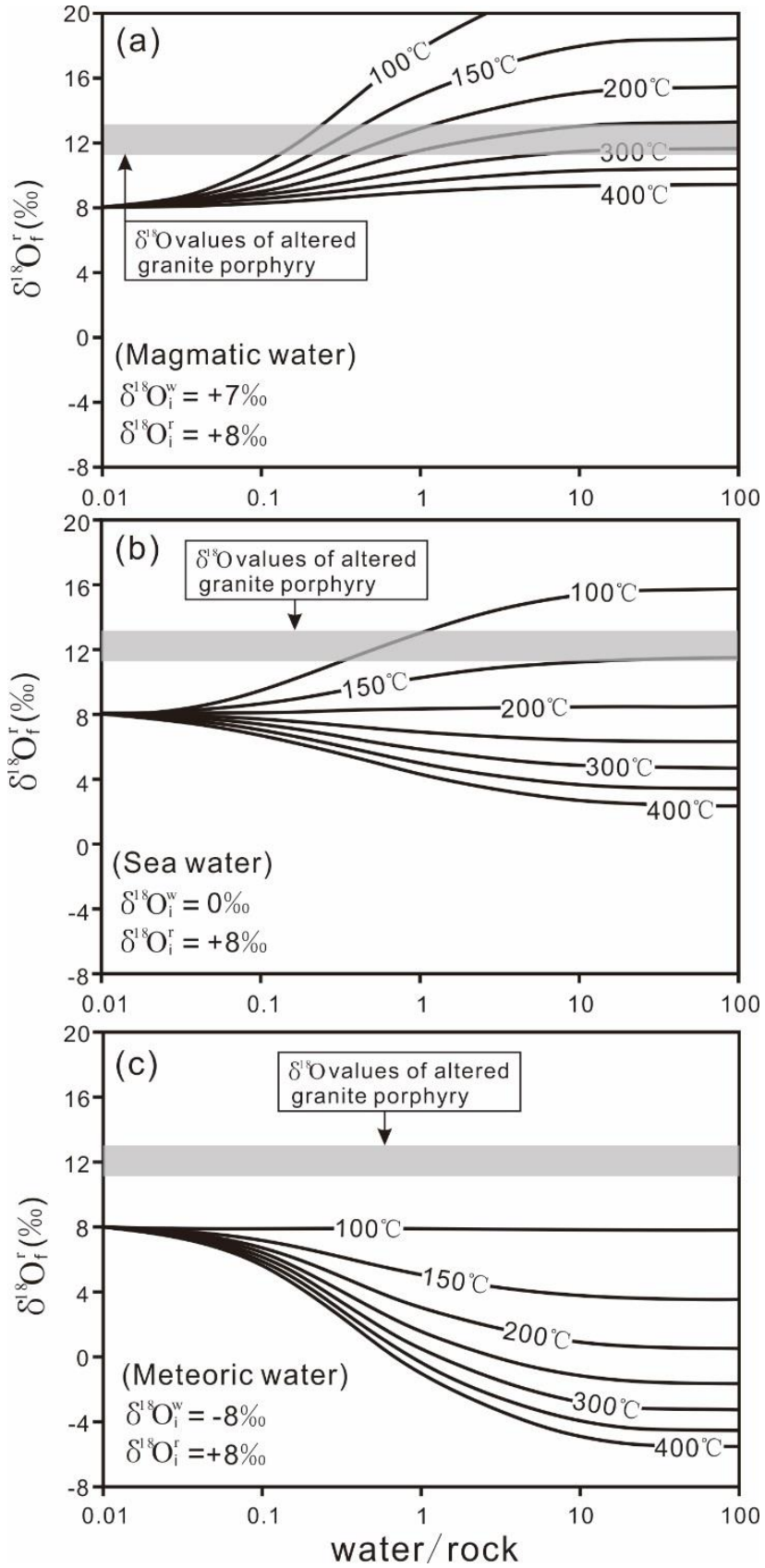

Fig. 28 Calculation of the final $\delta^{18}O$ values of rocks based on different initial water and temperature. $\delta^{18}O$ values of initial rock is +8‰. Shaded area indicated the $\delta^{18}O$ values of altered granite porphyry near pyrite quartz vein, pyrite-chalcopyrite quartz vein and sphalerite-galena quartz vein. (a) $\delta^{18}O$ value of initial water is magmatic water. (b) $\delta^{18}O$ value of initial water is seawater. (c) $\delta^{18}O$ value of initial water is meteoric water.

3.5.2 Sulfur isotopic ratios

The $\delta^{34}S$ values of pyrite and galena from sphalerite-galena quartz veins range from +3.3 to +3.6‰ and -0.2 to +0.8‰ (Table 6), respectively. These $\delta^{34}S$ values are similar to $\delta^{34}S$ values of magmatic sulfur. The formation temperature of sphalerite-galena quartz veins could also be estimated on the basis of the $\delta^{34}S$ values of pyrite and galena that coexist in sphalerite-galena quartz veins and the fractionation factor between pyrite and sphalerite (Rye, 1974). The formation temperatures of sphalerite-galena quartz veins were estimated around 235°C (Table 6). The formation temperature that was estimated by the sulfur isotope ratios is in agreement with the formation temperatures estimated by fluid inclusions and the presence of illite as alteration minerals. The formation temperature of gold-bearing quartz veins of the Xiajinbao deposit is thought to be around 220 to 265°C.

Based on research on sulfur isotope ratios of sulfide minerals and related igneous rocks by Sato et al. (1992), there is an intimate relation between $\delta^{34}S$ values of sulfide minerals of ore deposits and $\delta^{34}S$ values of related igneous rocks. The ranges of $\delta^{34}S$ values of magnetite-series granitoids and $\delta^{34}S$ values of sulfide minerals of the mineral deposits associated with the magnetite-series granitoids are from -4 to +7‰ and from 0 to +10‰, respectively. On the other hand, the ranges of $\delta^{34}S$ values of ilmenite-series granitoids and $\delta^{34}S$ values of sulfide minerals of the mineral deposits associated with the ilmenite-series granitoids are from -11 to -5‰ and from -11 to -2‰, respectively (Sato et al., 1992). In the eastern part of the north margin of the North China Craton, the sulfide minerals of gold deposits associated with I-type granitoids also have $\delta^{34}S$ values from -2 to +8 ‰ (Li and Santosh, 2014). These signatures are similar to the signatures of $\delta^{34}S$ values of ores of granitoid affinity in Japan. The $\delta^{34}S$ values of sulfide minerals of the Xiajinbao deposit range from -3 to +8 ‰ with the mode of +4 ‰ (Fig. 29). The distribution of sulfur isotope ratios of sulfide minerals of the Xiajinbao deposit are similar to the distribution of $\delta^{34}S$ values of ores associated with oxidized magma. This relation suggests that the ore-forming fluid that was associated with gold mineralization of the Xiajinbao deposit was derived from oxidized magma rather than reduced magma (Li et al., 2018). In the Xiajinbao mining area, there are acidic rocks such as granite porphyry, quartz porphyry dikes and basic rocks such as diorite dikes. The candidate of igneous rocks related to gold mineralization of the Xiajinbao deposit is thought to be diorite igneous activity. This idea is consistent with the fact that intense gold mineralization is observed near diorite dikes in the Xiajinbao deposit (Fig. 7). An understanding of the distribution of gold mineralization and distribution of mafic igneous rocks such as diorite is important for exploration of gold deposits

in east Hebei Province.

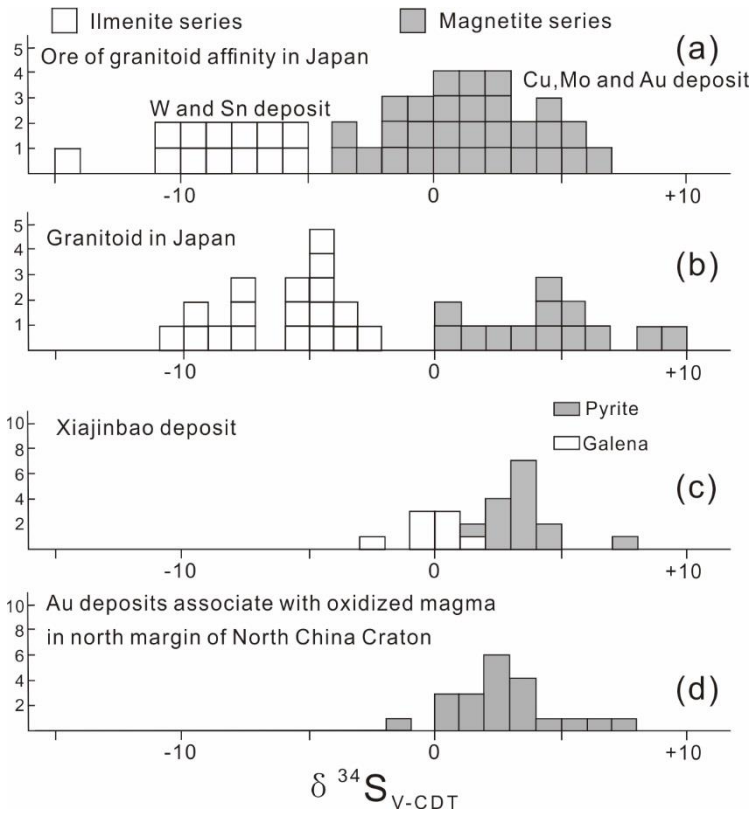

Fig. 29 (a) $\delta^{34}S$ values of ores of Cu, Mo and Au deposits associated with magnetite-series igneous activities and Sn and W deposits associated with ilmenite-series igneous activities (Sato et al., 1992). (b) $\delta^{34}S$ values of granitoid classified into magnetite-series and ilmenite-series granitoids (Sato et al., 1992). (c) $\delta^{34}S$ values of pyrite and galena of the Xiajinbao deposit. (d) $\delta^{34}S$ values of ores of Au deposits associated with oxidized magma in North China Craton. The sulfur isotopic ratios of ores of gold deposits associated with oxidized magma in north margin of North China Craton are from Li and Santosh (2014)

Table 6 Sulfur isotopic ratios of sulfide minerals and estimated formation temperatures of the Xiajinbao deposit.

Sample	$\delta^{34}S_{V\text{-}CDT}$ (‰)	$\delta^{34}S_{V\text{-}CDT}$ (‰)	Temperature (℃)	Remarks
Mineral	Pyrite	Galena		
S1	3.5	-0.1	235	This study
S2	3.4	-0.2	235	This study
S3	3.3	0.8	337	This study
S4	3.6	-0.2	222	This study
PD9	4.6	1.6		(1)
PD20	7.4	0.4		(1)
PD2-Py2	4.3			(2)
PD2-Ga-Py	3.2			(2)
PD2-Py1	2.4			(2)
LT(882)04	1.9			(2)
PD516-2	3.0			(2)
PD516-4	2.2			(2)
PD516-7	2.9			(2)
PD516-9	2.0	0.9		(2)
PD516-11	3.1			(2)
LT(882)05		-2.1		(2)

(1) Yang (1983), (2) Hebei Bureau of geology and mineral resources exploration (1992)

3.6 Formation environment of the Xiajinbao deposit

3.6.1 Formation temperature

The formation temperature of the Xiajinbao deposit can be summarized in three aspects: 1) presence of illite as the main alteration mineral suggest the formation of gold-bearing quartz veins were formed above 200 ºC, 2) the homogenization temperature of the fluid inclusion indicate 175 to 260 ºC, and 3) $\delta^{34}S$ values of pyrite and galena that coexist in sphalerite-galena quartz suggest the equilibrium temperature is around 235 °C. On the basis of these facts, the sulfur fugacity can be estimated base on the mineral assemblages, formation temperature and chemical component of sphalerite.

3.6.2 Sulfur fugacity

The sulfur fugacity during the period of formation of sphalerite-galena quartz veins was estimated on the basis of the FeS content in sphalerite and thermodynamic data (Barton and Toulmin, 1966). The FeS contents of sphalerite in sphalerite-galena quartz veins of the

Xiajinbao deposit range from 0.4 to 7.1 mol % FeS (Fig. 30). The sulfur fugacity of the Xiajinbao deposit was estimated to be from $10^{-10.2}$ to $10^{-13.6}$ atm based on the formation temperatures estimated by homogenization temperature of fluid inclusions in sphalerite-galena quartz veins (Fig. 30) (Li et al., 2018). The estimated environment is similar to the intermediate sulfidation condition of Pb-Zn-Ag zoned base metal vein related to oxidized magma (Einaudi et al., 2003).

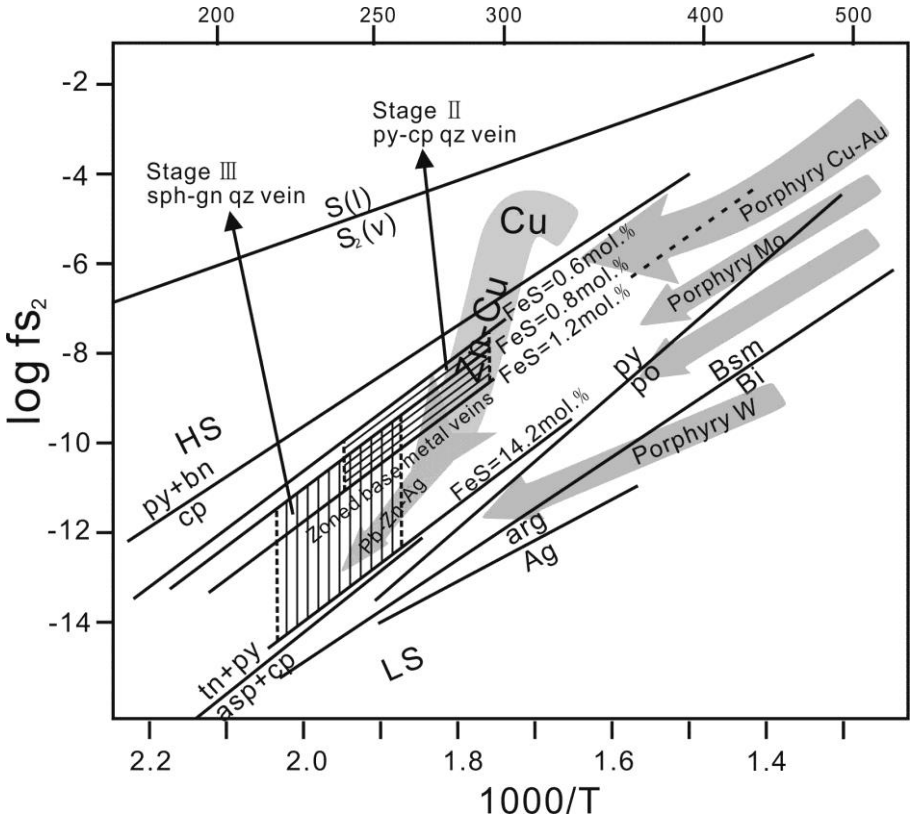

Fig. 30 Sulfur fugacity versus temperature diagram showing the depositional conditions of sphalerite-galena quartz vein of the Xiajinbao deposit based on the mineral assemblages, chemical composition of sphalerite and homogenization temperature of fluid inclusions. Hatched area indicates environment for formation of the sphalerite-galena quartz vein of the Xiajinbao deposit. The shaded area corresponds to evolution of environments of ore-forming fluid associated with andesitic magma and reduced-type magma that proposed by Einaudi et al. (2003). The sources of stability curves; isopleths (mole % FeS): Barton and Skinner (1979). Abbreviations: HS; high sulfidation epithermal mineralization, LS; low sulfidation epithermal mineralization.

Table 7 Chemical compositions of sphalerite in pyrite-chalcopyrite quartz veins and sphalerite-galena quartz veins of the Xiajinbao deposit.

wt.%	1	2	3	4	5	6	7	8	10	11	12	13	14	15	16	17	18
Zn	66.9	67.1	66.4	64.9	65.2	64.4	66.3	66.5	65.5	63.4	63.3	65.9	64.6	66.7	65.7	58.5	59.2
Fe	0.3	0.3	0.6	1.6	1.7	3.1	0.8	0.4	1.8	3.5	3.2	1.2	3.0	0.5	1.0	8.4	7.4
Mn	-	-	-	-	-	-	-	-	-	0.1	-	-	-	-	-	0.2	0.2
Cd	0.9	0.9	0.9	0.6	0.6	1.0	1.6	1.6	0.7	0.9	1.0	0.9	0.7	1.0	0.9	0.8	0.9
Cu	0.3	0.2	0.5	0.3	0.2	-	-	0.2	-	0.1	0.4	-	-	0.1	0.3	-	-
In	-	-	-	-	-	-	-	-	-	-	-	-	-	-	-	-	-
Ga	-	0.1	0.1	-	-	-	0.1	-	0.1	0.1	-	-	0.1	0.1	-	0.1	0.1
S	32.8	33.1	33.0	33.1	33.3	33.5	33.1	33.1	33.3	33.0	33.4	33.6	33.2	33.4	33.3	33.7	33.8
Total	101.1	101.7	101.6	100.5	101.1	101.9	101.9	101.7	101.4	101.1	101.3	101.6	101.6	101.9	101.3	101.8	101.7
at.%																	
Zn	49.6	49.4	48.9	48.1	48.1	47.1	48.9	49.1	48.2	46.8	46.5	48.3	47.4	49.0	48.5	42.4	43.0
Fe	0.3	0.3	0.6	1.4	1.5	2.6	0.7	0.4	1.6	3.0	2.8	1.0	2.5	0.5	0.9	7.1	6.3
Mn	-	-	-	-	-	-	-	-	-	0.1	-	-	-	-	-	0.2	0.2
Cd	0.4	0.4	0.4	0.3	0.3	0.4	0.7	0.7	0.3	0.4	0.4	0.4	0.3	0.4	0.4	0.3	0.4
Cu	0.2	0.2	0.4	0.2	0.2	-	-	0.1	-	0.1	0.3	-	-	0.1	0.3	-	-
In	-	-	-	-	-	-	-	-	-	-	-	-	-	-	-	-	-
Ga	-	0.1	0.1	-	-	-	0.1	-	0.1	0.1	-	-	0.1	0.1	-	0.1	0.1
S	49.5	49.7	49.6	50.0	50.0	49.9	49.7	49.8	49.9	49.6	50.0	50.3	49.6	50.0	50.0	49.8	50.0

-: below detection limit. Nos. 1 to 3 are data of sphalerite from pyrite-chalcopyrite quartz vein. Nos. 4 to 18 are data of sphalerite from sphalerite-galena quartz vein.

Chapter 4 Introduction of Dongliang deposit

4.1 Geology of the Dongliang deposit

The Dongliang deposit is about 2km away from the southeast part of Xiajinbao deposit. The geology of the Dongliang mining area is similar to the Xiajinbao mining area, which consist of Proterozoic sedimentary rocks and Jurassic ingeous rocks. The igneous rocks in the Dongliang mining area include Tuff, granite porphyry, quartz porphyry and diorite (Fig. 31). A route map was carried out in the open pit of the Dongliang deposit (Fig. 32). The diorite cut the tuff in

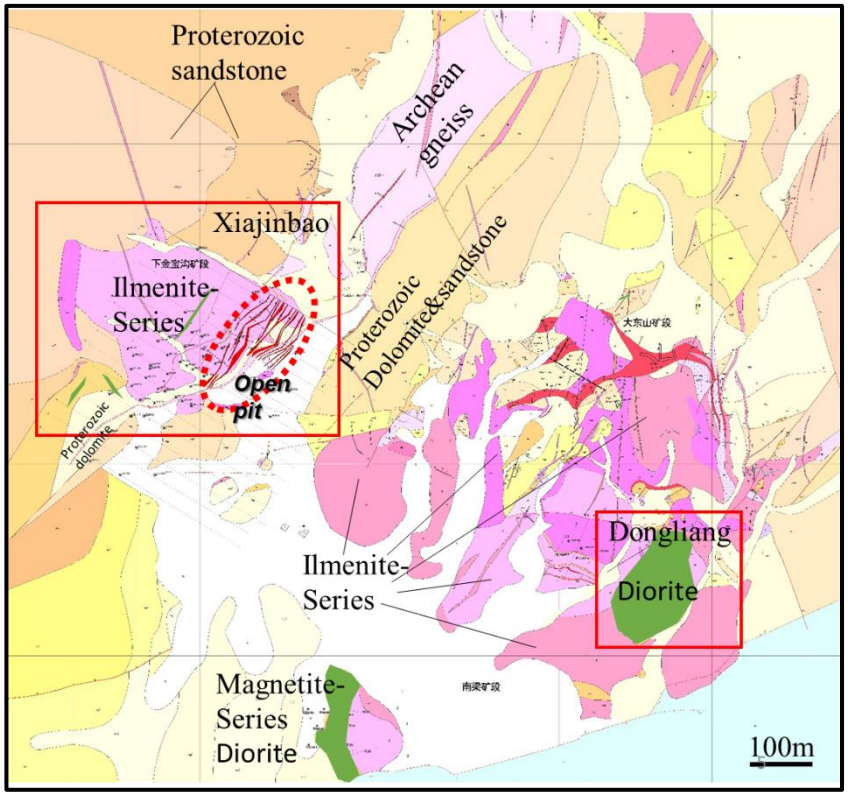

Fig. 31 Geologic map in the open pit of the Dongliang deposit.

the east part of the Dongliang area. Many quartz porphyry dikes occur in the diorite. Based on the cross-cutting relationship between those igneous rocks in the Dongliang deposit, the emplacement sequence was summarized from old to younger as follows: Tuff, granite porphyry, diorite and quartz porphyry. The orebodies in the Dongliang deposit were mainly hosted in the diorite. The orebodies were defined as containing over 0.8g/t Au. One west-east cross-section of the open pit is shown below.

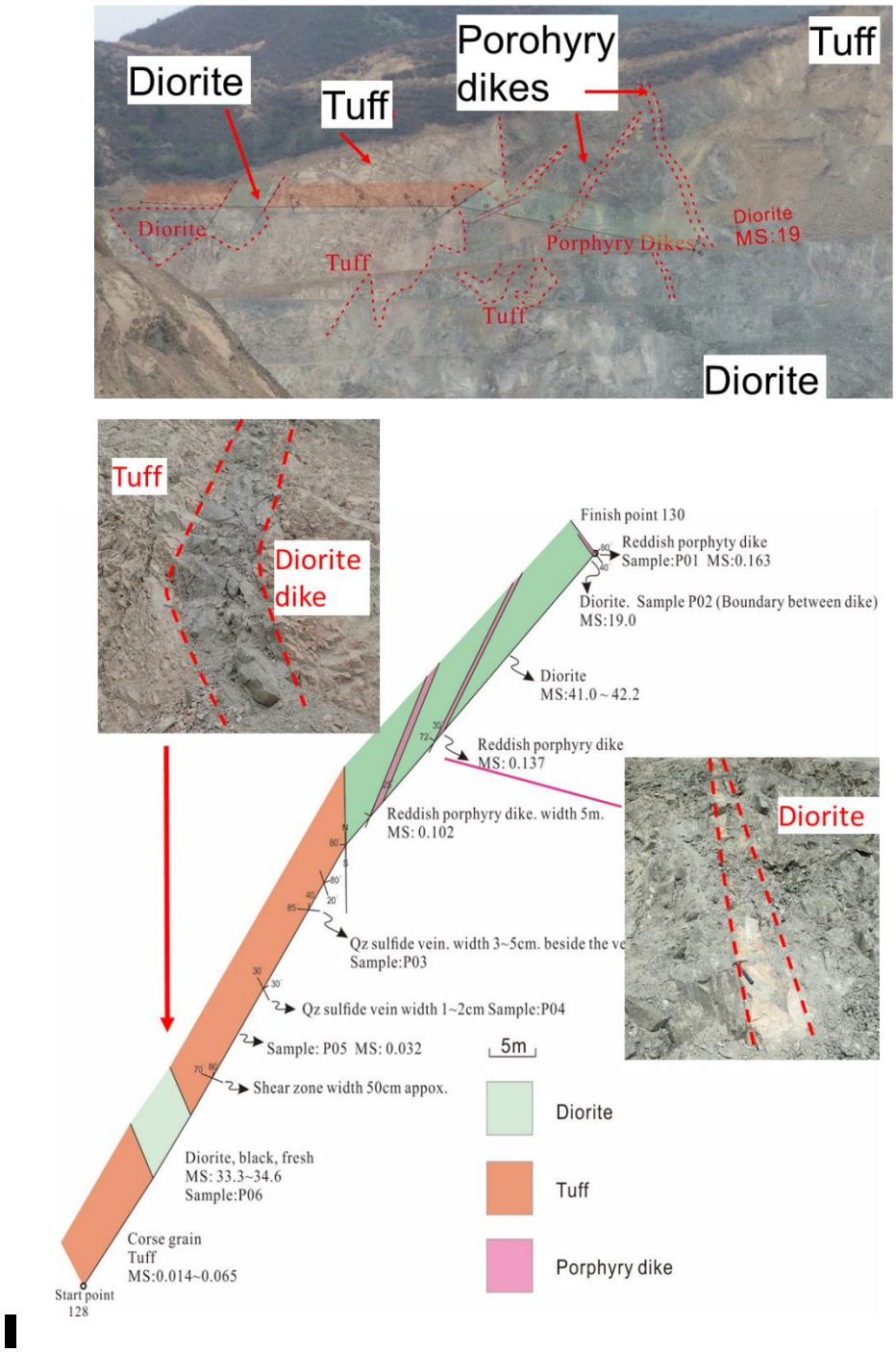

Fig. 33 Photo and route map shows the cross-cutting relationship in the open pit of the Dongliang deposit.

4.2 Geochemical characteristics of the igneous rocks in the Dongliang deposit

The chemical composition of the tuff, diorite, and porphyry dike were also determined. The results were shown in Table 8.

The aluminum saturation index of the tuff in the Dongliang deposit was 1.03 while the diorite in the Dongliang deposit range from 0.84 to 0.88. The porphyry dike sample P01 having

aluminum saturation index around 0.61 was interpreted as strongly altered. The magnetic susceptibility of these rocks was also measured. The diorite in the Dongliang deposit having a magnetic susceptibility from 16 to 60×10^{-3} SI unit while the tuff, granite porphyry and porphyry dikes were all lower than 1×10^{-3} SI unit (Fig. 33). The magnetic susceptibility suggests that in the Dongliang deposit, the diorite belongs to magnetite-series while the tuff, granite porphyry and porphyry dikes belong to ilmenite-series.

Table 8 Chemical compositions of the igneous rocks in the Dongliang deposit.

Sample	P131	P01	P05	125-2	P06	125-4
wt%	DL-porphyry dike	DL-porphyry dike	DL-tuff	DL-tuff	DL-diorite	DL-diorite
SiO_2	70.46	65.42	70.98	70.67	54.08	55.10
TiO_2	0.20	0.17	0.20	0.20	0.92	0.94
Al_2O_3	13.25	12.24	14.02	14.19	17.36	17.68
TFe_2O_3	1.15	0.88	0.87	1.23	8.86	7.74
MnO	0.07	0.16	0.02	0.04	0.14	0.12
MgO	0.96	0.71	0.43	0.51	2.62	2.58
CaO	1.87	5.96	1.46	1.36	6.21	5.85
Na_2O	2.75	2.33	3.26	3.44	4.55	4.43
K_2O	5.33	5.14	5.15	5.27	1.73	1.98
P_2O_5	0.07	0.07	0.07	0.08	0.28	0.28
H_2O (-)	0.33	0.38	0.43	0.29	0.24	0.32
LOI	3.39	6.39	2.66	2.56	2.83	2.79
FeO	-	-	-	-	-	-
Total	99.8	99.9	99.6	99.8	99.8	99.8
ppm						
Zr	167.00	159.00	169.00	167.00	155.00	158.00
ASI	0.97	0.61	1.03	1.03	0.84	0.88

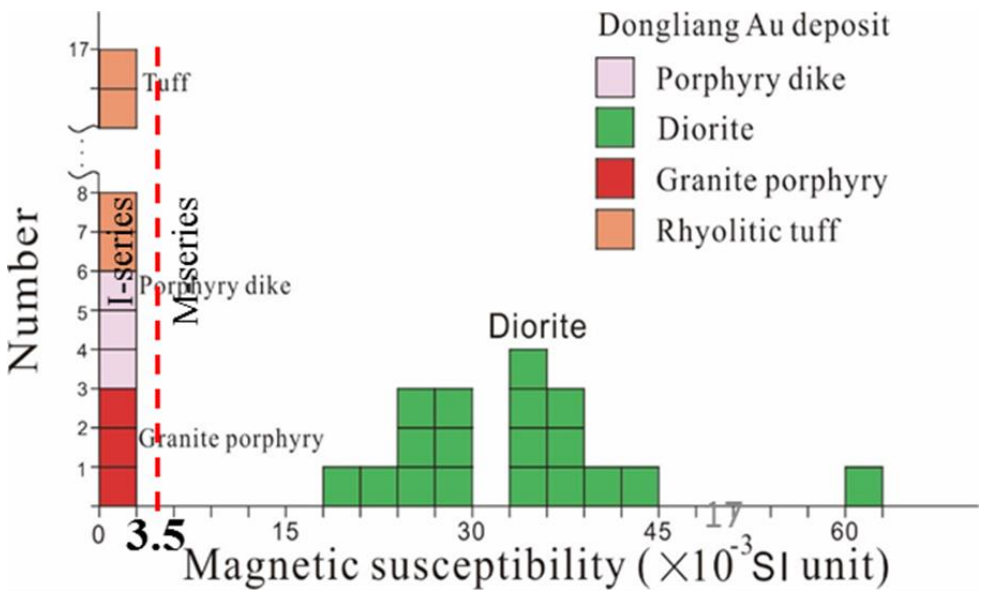

Fig. 35 Magnetic susceptibility of the igneous rocks in the Dongliang deposit

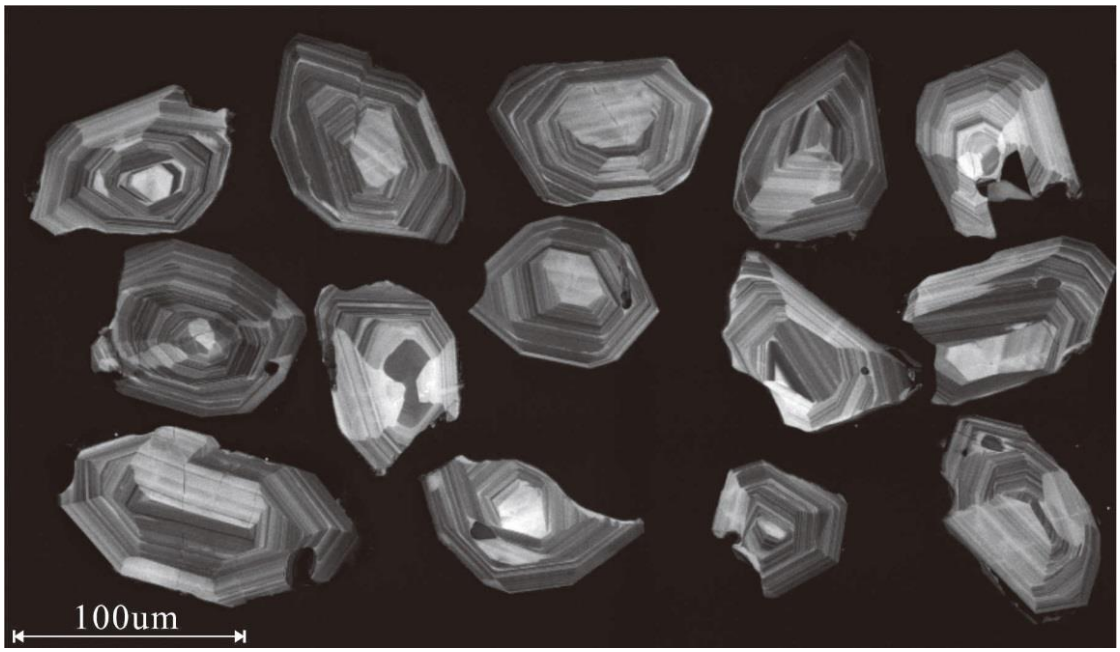

Fig. 34 CL photomicrograph of Zircon in the tuff of the Dongliang deposit.

The age of the tuff, diorite, and porphyry dike in the Dongliang deposit were also determined by zircon U-Pb isotope geochronology method. The zircon in the tuff shows euhedral shape and clearly oscillatory zoning similar to the zircon in the granite porphyry of the Xiajinbao deposit (Fig. 34). The zircon in the diorite of Dongliang deposit was separated into two groups. One group shows euhedral shape and clearly oscillatory zoning, some zircon can also have alteration zoning near the outer margin (Fig. 35). Another group shows dark gray to black color

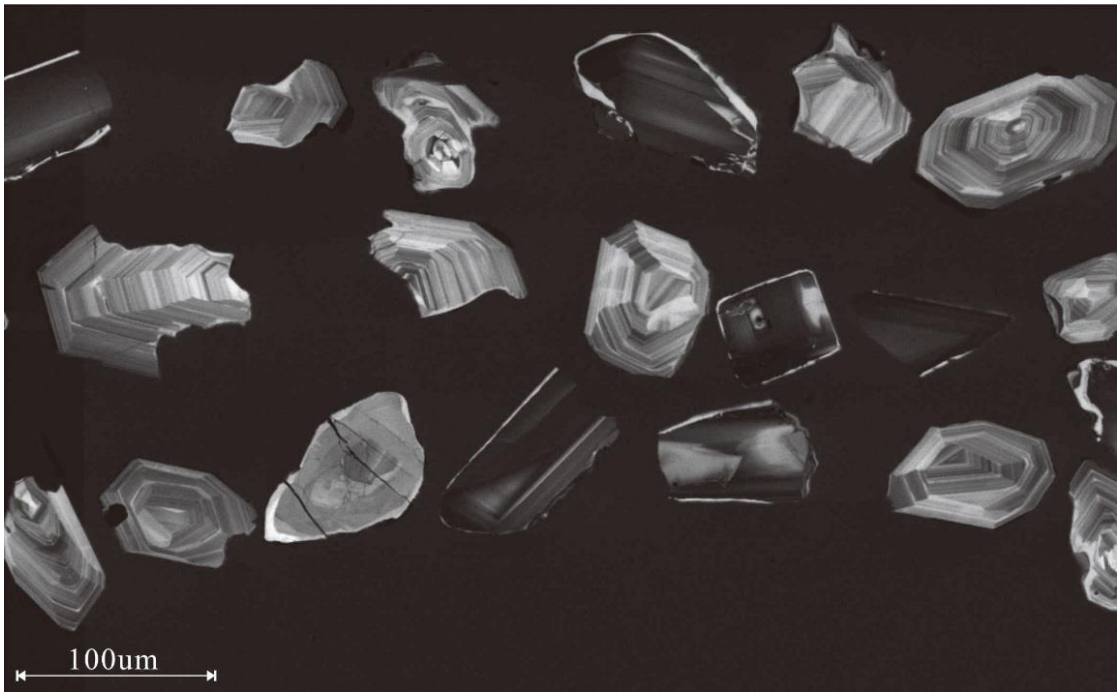

Fig. 38 CL photomicrograph of Zircon in the diorite of the Dongliang deposit.

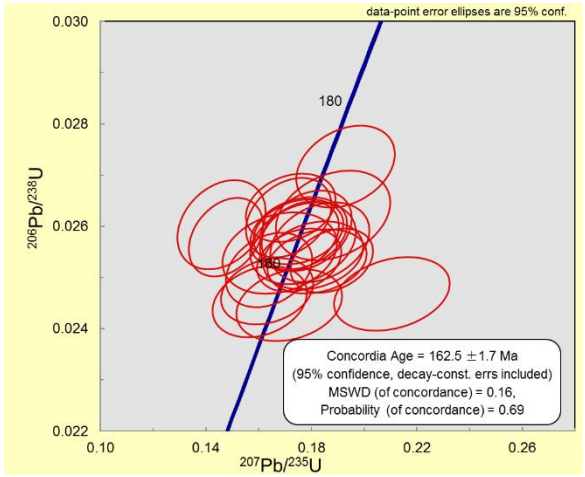

Fig. 36 Concordia age of the tuff of the Dongliang deposit.

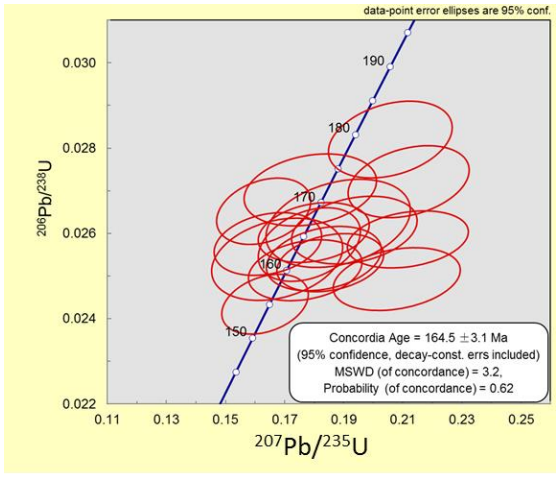

Fig. 37 Concordia age of the diorite of the Dongliang deposit.

without oscillatory zoning. Several points on the second group zircon were selected for age dating. The result shows trace of them having similar age data compare with the first group while others have very different results. There is a possibility that those kinds of zircon having similar age may be caused by special cutting of lattice plane while the others may be caused by a different source(s) that needs to be figured out in the future.

The concordia age of the tuff is 162.5±1.7Ma. The concordia age of the diorite is 164.5±3.1Ma. The age of the tuff and diorite in the Dongliang deposit is very similar to the granite porphyry and diorite dikes in the Xiajinbao deposit which suggest that these igneous rocks were formed almost in the same period (Figs. 36 and 37).

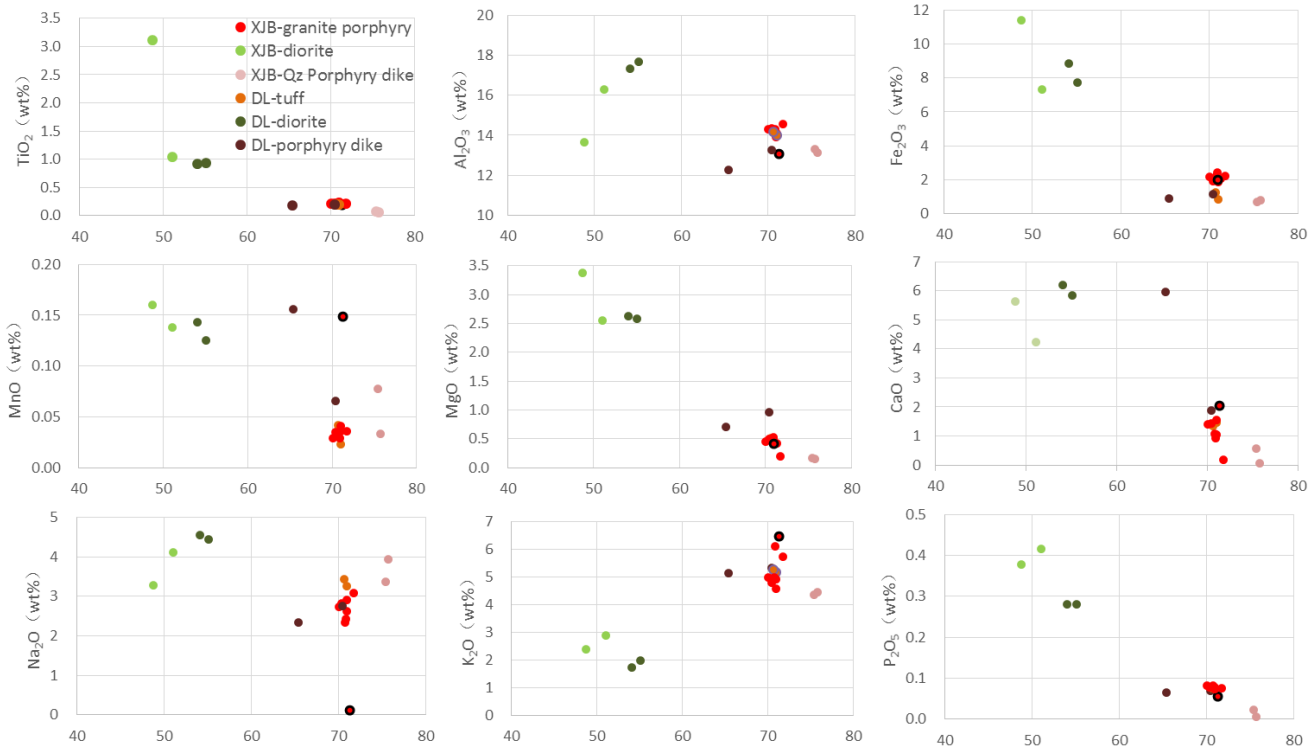

Fig. 39 Comparison of the major elements of igneous rocks between Xiajinbao deposit and Dongliang deposit

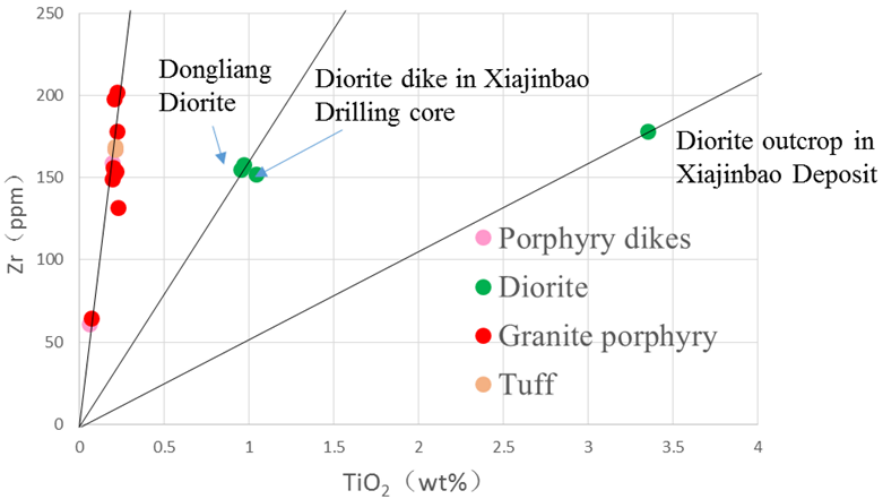

Fig. 40 Comparison of TiO2 vs Zr diagram of igneous rocks between Xiajinbao deposit and Dongliang deposit.

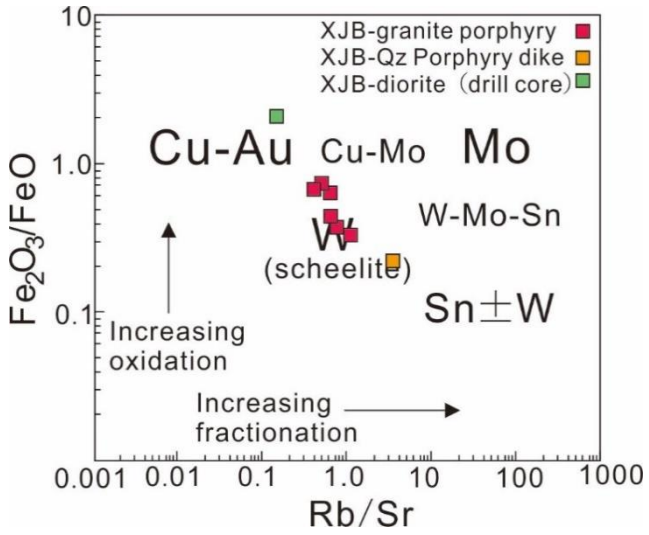

Fig. 41 Diagram of Fe_2O_3/FeO versus Rb/Sr ratios showing the comparisons among the igneous rocks in Xiajinbao deposit porphyry system.

4.3 Comparison between Xiajinbao deposit and Dongliang deposit

The Xiajinbao deposit and the Dongliang deposit are 2km apart. The geologic characteristics are consistent between these two deposits. The occurrence of the orebodies in the Dongliang deposit suggests that the diorite in the mining area has potential for gold mineralization. The igneous rock in these two deposits also shows similar chemical component. The Harker diagram suggests that some major elements changed during the hydrothermal alteration (Fig. 38). However, the immobile elements such as Ti and Zr concentration did not change during the hydrothermal alteration. In the TiO_2-Zr diagram, the diorite dike in the Xiajinbao deposit and the diorite in the Dongliang deposit shows similar TiO_2-Zr ratios while the quartz porphyry dike, granite porphyry in the Xiajinbao deposit, and the tuff, granite porphyry, porphyry dikes in the Dongliang deposit have another TiO_2-Zr ratio and almost plot in one single line (Fig. 39). These facts suggest that the diorite dike in the Xiajinbao deposit and the diorite in the Dongliang deposit may be derived from same or similar source.

The mineralization largely depends on physico-chemical conditions. In the porphyry system, the type of mineralization largely depends on oxidation states. Ishihara (1977) proposed the boundary between magnetite-series and ilmenite-series. Thompson et al. (1999) discussed the relation between element association and oxidization state. Generally, with the decrease in oxidation state and increase in fractionation, the type of mineralization changes through Cu-Au, Cu-Mo to W-Mo-Sn type (Sillitoe, 2010; Sun et al., 2015). Comparing the igneous rocks from Xiajinbao deposit and the porphyry system, it is clear that the diorite is associated with the Cu-Au mineralization whereas the granite porphyry and quartz porphyry are associated with W mineralization, which tends to transform into Sn±W mineralization (Fig. 40).

Chapter 5 Summary

(1) The igneous activity of the Xiajinbao mining area is characterized by bimodal igneous activities of ilmenite-series granite porphyry and quartz porphyry dikes and magnetite-bearing diorite dikes. The distribution of bonanza of gold mineralization of the Xiajinbao deposit is present near the diorite dikes in the granite porphyry.

(2) The granite porphyry in Xiajinbao deposit was formed in 157 Ma. The zircon in the granite porphyry show magmatic characteristics.

(3) The formation temperature of gold-bearing sulfide quartz veins ranges from 220 to 260 °C. The formation temperature and $\log fs_2$ of the sphalerite-galena quartz vein are similar to the formation environment of an intermediate sulfidation condition of Pb-Zn-Ag zoned base metal vein associated with oxidized magma. The $\delta^{18}O$ and δD values of ore-forming fluid for gold mineralization of the sphalerite-galena quartz vein show a signature of magmatic water. The sulfur isotope ratios of sulfide minerals of the Xiajinbao deposit also suggest that the gold mineralization in the Xiajinbao deposit is related to oxidized magma. These facts suggest that gold mineralization of the Xiajinbao deposit was formed by oxidized igneous activity.

Fig. 42 Comparison of the major elements of igneous rocks between Xiajinbao deposit and Dongliang deposit

Acknowledgments

I would like to acknowledge and thank the following people for their contribution to this research: Professor Emeritus Osamu Matsubaya (Akita University) for helping with stable isotope analysis, Professor Ishiyama Daizo and Assistant Professor Mayuko Fukuyama (Akita University) for discussion during the research. I also thank the manager and staff of Jinbao Mining Company for allowing us access to the deposit to conduct the field survey and sampling. I am grateful to the Society of Resource Geology for support of travel expenses to China for the field survey in 2016.

References

Barton, P. B. and Skinner, B. J. (1979) Sulfide mineral stabilities, *in* Barnes, H. L., ed., Geochemistry of hydrothermal ore deposits: Holt, Rinehart and Winston, New York, 278-403.

Barton, P. B. and Toulmin, P. (1966) Phase relations involving sphalerite in the Fe-Zn-S system, Econ. Geol., 61, 815-849.

Bodnar, R. J. (1993) Revised equation and table for determining the freezing-point depression of H_2O-NaCl solution, Geochim. Cosmochim. Acta, 57, 683-684.

Chappell, B. W. and White, A. J. R. (1992) I- and S-type granites in the Lachlan Fold Belt, Special Paper of the Geological Society of America, 272, p. 1-26.

Chen, J. and Dong, J. (1993) Metallogenic map of gold deposits in China (1:4,000,000) and its legend. Beijing internal report, Institute of Gold Geology, Ministry of the Metallurgical Industry, (in Chinese)

Craig, H. (1961) Isotopic variations in meteoric waters, Science, 133, 1702-1703.

Deng, F. (2014) Brief analysis on the Xiajinbao gold deposit in Xiayingfang mining area, Hebei, Western Exploration Engineering, 9, 139-140+143.

Einaudi, M. T., Hedenquist, J. W., and Inan, E. E. (2003, Sulfidation state of fluids in active and extinct hydrothermal systems: transitions from porphyry to epithermal environments, Society of Economic Geologists and Geochemical Society, Giggenbach Volume Special Publication 10, 1-50.

Giggenbach, W. F. (1992) Isotopic shift in waters from geothermal and volcanic systems along convergent plate boundaries and their origin, Earth Planet. Sci. Lett., 113, 495-510.

Hart, C. J. R., Goldfarb, R. J., Qiu, Y., Snee, L., Miller, L. D., and Miller, M. L. (2002) Gold deposits of the northern margin of the North China Craton: multiple late Paleozoic–Mesozoic mineralizing events, Mineral. Deposita, 37, 326-351.

Hebei Bureau of geology and mineral resources exploration (1992) Report of geological exploration of Xiajinbao deposit in Xiayingfang gold mining area, 66p (In Chinese)

Henley, R. W., Truesdell, A. H., Barton, P., Jr. and Whitney, J. A. (1984) Fluid-mineral equilibria in hydrothermal systems, Society of Economic Geologists, Reviews in Economic Geology, 1, 267.

Ishikawa, Y., Sawaguchi, T., Iwaya, S. and Horiuchi, M. (1976) Delineation of prospecting targets for Kuroko deposits based on modes of volcanism of underlying dacite and alteration halos, Mining Geology, 26, 105-117.

Kita, I. and Matsubaya, O. (1983) F2-technique for the oxygen isotopic analysis of silica minerals, Akita Daigaku Kozangakubu Chika Shigen Kenkyushisetsu Hokoku, 25-33.

Large, R. R., Gemmell, J. B., and Paulick, H. (2001) The alternation box plot: A simple approach to understanding the relationship between alteration mineralogy and lithogeochemistry associated with volcanic-hosted massive sulfide deposits, Econ. Geol., 96, 957-971.

Lei, S., Li, Y., and Hu, J., (1995a) Geological Features, Forming Conditions and Magmatism and Mineralization Controlling of S-shaped Asymmetrical Fold in Xiayingfang Distric, Pingquan, NE Hebei, China, Journal of Hebei College of Geology, 18, 11-19.

Lei, S., Li, Y. and Hu, J. (1995b) Identification of S-type Asymmetrical fold and its action on controlling magmatism and mineralization in Xiayingfang District, Pingquan, Hebei Province, Journal of Graduate School, China University of Geosciences, 9, 459-466.

Li, M., Chai, F., Ye, H., Su, H., Lu, D., Zhang, L., and Zhang, H. (2016) The geochemical characteristics, LA-ICP-MS Zircon U-Pb age dating, Hf isotope and other geologic meaning of Jingbaogou granite porphyry in Jidong, Geological Bulletin of China, 35, 790-806.

Li, S. R. and Santosh, M. (2014) Metallogeny and craton destruction: Records from the North China Craton, Ore Geol. Rev., 56, 376-414.

Li, H., Ishiyama, D., Zhang, Y., and Shao, Y. (2018) geology and geochemical characteristics of the Xiajinbao gold deposit in the Hebei Province, China. J. Mineral. Petrol. Sci., 113,24-40.

Liu, C., Nie, F., and Bagas, L. (2016) Geology and ore genesis of the Yu'erya gold deposit, eastern Hebei Province, China, Ore Geol. Rev., 73, 270-283.

Luan, W. and Yu, Y. (1995) Geochemistry of fluid inclusion of Xiayingfang gold deposit in Pingquan of Hebei Province and Ore-Searching significance, Journal of Precious metallic geology, 4, 161-167.

Ludwig, K. R. (2003) Isoplot 3.00, Berkeley Geochronology Center Special Publication, 4, 70.

Marumo, K., Longstaffe, F. J., and Matsubaya, O. (1995) Stable isotope geochemistry of clay minerals from fossil and active hydrothermal systems, southwestern Hokkaido, Japan, Geochim. Cosmochim. Acta, 59, 2545-2559.

Matsuhisa, Y., R.Goldsmith, J., and Clayton, R. N. (1979) Oxygen isotopic fractionation in the system quartz-albite-anorthite-water, Geochim. Cosmochim. Acta, 43, 1131-1140.

Miao, L. C., Qiu, Y. M., McNaughton, N., Luo, Z. K., Groves, D., Zhai, Y. S., Fan, W. M., Zhai, M. G., and Guan, K. (2002) SHRIMP U-Pb zircon geochronology of granitoids from Dongping area, Hebei Province, China: constraints on tectonic evolution and geodynamic setting for gold metallogeny, Ore Geol. Rev., 19, 187-204.

Nie, F. J., Jiang, S. H., and Liu, Y. (2004) Intrusion-related gold deposits of North China craton, People's Republic of China, Resour. Geol., 54, 299-324.

O'Neil, J. R. and Taylor, J. (1967) The oxygen isotope and cation exchange chemistry of feldspar, Am. Mineral., 52, 1414-1437.

Ohmoto, H. (1986) Stable isotope geochemistry of ore deposits, Rev. Mineral., 16, 491-560.

Qiu, X., Hu, S., Wang, J., and Wang, S. (1997) Gold mineralization of Xiaoyingpan quartz-carbonate gold deposit, Hebei Province, Acta Geol. Sin., 71, 350-359.

Rye, R. O. (1974) A comparison of sphalerite-galena sulfur isotope temperatures with filling temperatures of fluid inclusions, Econ. Geol., 69, 26-32.

Santosh, M. (2010) Assembling North China Craton within the Columbia supercontinent: The role of double-sided subduction, Precambrian Res., 178, 149-167.

Santosh, M., Liu, D., Shi, Y., and Liu, S. J. (2013) Paleoproterozoic accretionary orogenesis in the North China Craton: A SHRIMP zircon study, Precambrian Res., 227, 29-54.

Sato, H., Ishiyama, D., Mizuta, T., and Ishikawa, Y. (1999) Rare earth element analysis of rock thermal water samples by inductively coupled plasma mass spectrometry (ICP-MS), Scientific and Technical Reports Faculty of Engineering and Resource Geology, Akita University, 20, 8.

Sato, K., Ishihara, S., and Shibata, K. (1992) Granitoid map of Japan. Geological atlas of Japan (2nd ed.), Geological survey of Japan.

Sheppard, S. M. F. and Gilg, H. A. (1996) Stable isotope geochemistry of clay minerals, Clay Minerals, 31, 1-24.

Sillitoe, R. H. (2010) Porphyry Copper Systems, Econ. Geol., 105, 3-41.

Song, Y., Jiang, S. H., Bagas, L., Li, C., Hu, J. Z., Zhang, Q., Zhou, W., and Ding, H. Y. (2014) The geology and geochemistry of Jinchangyu gold deposit, North China Craton: implications for metallogenesis and geodynamic setting, Ore Geol. Rev.

Sun, W., Huang, R.-f., Li, H., Hu, Y.-b., Zhang, C.-c., Sun, S.-j., Zhang, L.-p., Ding, X., Li, C.-y., Zartman, R. E., and Ling, M.-x. (2015) Porphyry deposits and oxidized magmas, Ore Geol. Rev., 65, Part 1, 97-131.

Sweatman, T. R. and Long, J. V. P. (1969) Quantitative electron probe microanalysis of rock-forming minerals, J. Petrol, 10, 332-379.

Tang, P., Wang, J., and Wang, Y. (2009) The geology, ore-controlling and exploration of Xiayingfang mining area, Hebei Province, Mineral academic journal, S1, 560-561.

Taylor, B. E. (1992) Degassing of H_2O from rhyolite magma during eruption and shallow inrusion, and the isotopic composition of magmatic water in hydrothermal systems, Geological Survey Japan, 279, 190-194.

Taylor, H. P., Jr. (1971) Oxygen isotope evidence of large-scale interaction between meteoric ground waters and Tertiary granodiorite intrusions, western Cascade Range, Oregon, Geophys. Res., 76, 7855–7874.

Wang, B., Niu, S., Sun, A., and Li, H. (2003) Isotopic characteristics of Mesozoic Au-Ag

polymetallic ore deposits in Northern Hebei and their ore-forming materials source, Chin. J. Geochem., 22, 203-214.

Xu, E. S., Jin, Y. G., Zhu, F. S., Wang, X. Z., and Yang, L. S. (1992) Gold, silver, and platinoid deposits of China., *in* China, i. E. C. o. M. D. o., ed., Mineral Deposits of China, Beijing Geological Publishing House, p. 294-349.

Yang, T. (1983) The characteristics of Xiayingfang gold mineralization in Hebei Province, Geol. Sci. Tech. Inform., 139-147.

Ye, M. (2013) Simple analysis on the genesis of Xiayingfang gold deposit in Pingquan, Hebei province, Engineering design and research, 135, 6-8+17.

Yuan, W., Wang, S., and Wang, L. (1999) Fission track study on the metallogenetic age of Xiayingfang gold deposit in eastern Hebei, Nuclear Techniques, 22, 411-413.

Zhai, M. (2014) Multi-stage crustal growth and cratonization of the North China Craton, Geoscience Frontiers, 5, 457-469.

Zhang, J., Shao, Y., Liu, Z., Wang, C., Zou, Y., and Li, H. (2016) Zircon U-Pb geochronology and Hf isotope characteristics of Xiaojinbao granite-porphyry body, Hebei Province, and its geological significance, The Chinese Journal of Nonferrous Metals, 26, 137-148.

Zhang, J., Shao, Y., Wang, C., Liu, Z., and Xiong, Y. (2017) Ore-forming mechanism of Xiajinbao gold deposit in Pingquan, Hebei based on fluid inclusions and stable isotopes, Transactions of Nonferrous Metals Society of China, 27, 1363-1373.

Zhang, W., Qing, M., Niu, C., Wang, K., Huang, H., and Wang, M. (2014) An overview on type, spatial-temporal distribution and prospecting of gold deposits in China, Bull. China Soc. Mineral. Petrol. Geochem., 33, 721-732.

Zhao, G., Wilde, S. A., Cawood, P. A., and Sun, M. (2001) Archean blocks and their boundaries in the North China Craton: Lithological, geochemical, structural and P-T path constraints and tectonic evolution, Precambrian Res., 107, 45-73.

Zou, T., Wang, Y., Wang, J., Zhang, H., Zhao, L., Xie, H., Shi, Y., Liu, Y., and Liu, G. (2016) Geochronology of the Xiayingfang Au Deposit in Eastern Hebei Province, Geology and Exploration, 52, 84-97.

Appendix: LA-ICP-MS Th-U-Pb analytical data of zircon

	Th 232 ppm	U 238 ppm	Pb Total ppm	Pb Common Pb ppm	$^{207}Pb/^{206}Pb$ Ratio	$^{207}Pb/^{206}Pb$ 1σ	$^{207}Pb/^{235}U$ Ratio	$^{207}Pb/^{235}U$ 1σ	$^{206}Pb/^{238}U$ Age (Ma)	$^{206}Pb/^{238}U$ 1σ(Ma)
P05-01	106	205	6.65		0.0514	0.0034	0.1929	0.0123	173	3.3
P05-02	103	169	5.41	0.73	0.0476	0.0042	0.1680	0.0143	162	3.3
P05-03	117	178	5.83	1.33	0.0487	0.0036	0.1639	0.0108	160	3.0
P05-04	219	291	9.73	1.53	0.0544	0.0033	0.1877	0.0103	161	2.6
P05-05	149	223	7.56	1.24	0.0481	0.0035	0.1721	0.0112	168	2.8
P05-06	156	252	8.29	4.16	0.0493	0.0034	0.1751	0.0112	165	2.6
P05-07	188	272	8.95	0.14	0.0506	0.0035	0.1753	0.0105	161	2.6
P05-08	144	215	7.15	0.79	0.0491	0.0036	0.1752	0.0121	165	2.9
P05-09	177	256	8.46	1.41	0.0529	0.0038	0.1821	0.0124	161	2.6
P05-10	155	239	7.82	0.88	0.0523	0.0036	0.1807	0.0125	162	2.8
P05-11	105	191	5.84	0.089	0.0626	0.0046	0.2105	0.0145	157	3.0
P05-12	201	254	8.25	1.29	0.0487	0.0038	0.1632	0.0115	157	2.7
P05-13	212	288	9.75		0.0503	0.0031	0.1755	0.0099	164	2.8
P05-14	136	222	7.18	0.91	0.0420	0.0032	0.1459	0.0110	166	3.6
P05-15	128	214	6.95	0.49	0.0420	0.0028	0.1476	0.0093	164	3.2
P05-16	95.7	205	6.33		0.0509	0.0041	0.1768	0.0132	163	3.3
P05-17	115	179	5.92	1.80	0.0513	0.0036	0.1832	0.0124	164	3.2
P05-18	102	206	6.34		0.0498	0.0042	0.1716	0.0132	156	2.9
P05-19	102	207	6.27	0.93	0.0481	0.0039	0.1604	0.0118	156	2.9
P05-20	246	260	9.35	1.27	0.0484	0.0033	0.1714	0.0107	167	3.2
P05-21	170	211	7.43	0.38	0.0505	0.0036	0.1782	0.0113	165	3.3
P05-22	101	180	5.84		0.0535	0.0044	0.1882	0.0143	167	3.6
P06-01	30.5	154	17.09	0.33	0.0627	0.0027	0.8290	0.0347	587	9.8
P06-02	99.4	139	6.993	0.98	0.0573	0.0041	0.3580	0.0217	293	5.5
P06-04	50.6	104	3.32	0.15	0.0534	0.0057	0.1881	0.0161	167	4.3
P06-03	169	219	7.38		0.0519	0.0038	0.1783	0.0114	164	3.6
P06-05	136	219	7.80	1.15	0.0550	0.0041	0.2058	0.0138	179	3.7

Appendix: LA-ICP-MS Th-U-Pb analytical data of zircon

	Th 232 ppm	U 238 ppm	Pb Total ppm	Pb Common Pb ppm	$^{207}Pb/^{206}Pb$ Ratio	$^{207}Pb/^{206}Pb$ 1σ	$^{207}Pb/^{235}U$ Ratio	$^{207}Pb/^{235}U$ 1σ	$^{206}Pb/^{238}U$ Age (Ma)	$^{206}Pb/^{238}U$ 1σ(Ma)
P06-06	119	123	61.1	1.74	0.1225	0.0041	6.1190	0.1903	1953	22.0
P06-07	132	209	7.04		0.0582	0.0041	0.2117	0.0135	165	2.8
P06-08	34.8	225	50.91		0.0934	0.0031	2.6534	0.0835	1183	18.6
P06-09	85.4	156	5.19		0.0496	0.0047	0.1787	0.0148	172	3.5
P06-10	126	216	7.26	1.32	0.0581	0.0040	0.2120	0.0135	173	3.5
P06-11	136	232	7.33	0.21	0.0537	0.0040	0.1833	0.0129	162	3.1
P06-12	153	236	7.86	0.77	0.0456	0.0033	0.1629	0.0105	169	3.2
P06-13	141	149	21.46	0.054	0.0620	0.0031	0.9317	0.0465	671	10.7
P06-14	114	206	6.45		0.0466	0.0037	0.1643	0.0120	164	3.1
P06-15	56.1	84.0	36.4	2.17	0.1140	0.0038	5.2611	0.1663	1811	21.6
P06-16	65.2	116	3.69	0.69	0.0518	0.0062	0.1675	0.0146	162	4.0
P06-17	166	252	8.37	0.65	0.0524	0.0040	0.1798	0.0124	166	2.9
P06-18	109	173	5.65	1.16	0.0622	0.0049	0.2079	0.0142	159	3.1
P06-19	116	189	6.27		0.0557	0.0046	0.1936	0.0140	166	3.3
P06-20	16.4	566	51.16	1.32	0.0596	0.0024	0.6841	0.0271	514	7.3
P06-21	44.8	136	25.66	0.59	0.0722	0.0030	1.5705	0.0592	932	12.1
P06-22	194	257	8.79		0.0537	0.0041	0.1854	0.0119	161	2.8
P06-23	64.7	537	50.35	0.79	0.0559	0.0019	0.6592	0.0219	529	6.8
P06-24	112	162	5.12		0.0394	0.0039	0.1314	0.0117	154	3.3
P06-25	125	216	6.88	1.47	0.0509	0.0040	0.1770	0.0127	160	3.0
P06-26	236	287	9.41	0.66	0.0496	0.0034	0.1634	0.0097	155	2.9
115-1-01	227	288	9.80	1.37	0.0462	0.0033	0.1640	0.0107	165	2.9
115-1-02	135	182	5.85		0.0575	0.0047	0.1854	0.0139	154	3.2
115-1-03	65.4	138	4.34	1.23	0.0500	0.0049	0.1795	0.0157	164	3.8
115-1-04	74.2	137	4.31	0.55	0.0568	0.0054	0.1843	0.0152	157	3.8
115-1-05	161	238	6.84		0.0397	0.0035	0.1442	0.0125	170	3.2
115-1-07	86.4	180	5.55	1.03	0.0544	0.0047	0.1827	0.0140	160	3.1

Appendix: LA-ICP-MS Th-U-Pb analytical data of zircon

	Th 232 ppm	U 238 ppm	Pb Total ppm	Pb Common Pb ppm	$^{207}Pb/^{206}Pb$ Ratio	$^{207}Pb/^{206}Pb$ 1σ	$^{207}Pb/^{235}U$ Ratio	$^{207}Pb/^{235}U$ 1σ	$^{206}Pb/^{238}U$ Age (Ma)	$^{206}Pb/^{238}U$ 1σ(Ma)
115-1-08	86.9	154	4.95		0.0492	0.0043	0.1765	0.0136	172	3.6
115-1-09	109	200	6.38	1.01	0.0575	0.0055	0.2004	0.0158	163	3.4
115-1-10	105	193	6.27	0.40	0.0570	0.0043	0.2022	0.0134	169	3.2
115-1-11	128	220	6.74	0.44	0.0371	0.0031	0.1286	0.0095	161	3.1
115-1-12	62.4	133	4.04	0.46	0.0549	0.0067	0.1760	0.0185	163	3.6
115-1-13	88.1	186	6.19	0.88	0.0605	0.0042	0.2234	0.0134	175	3.4
115-1-14	83.4	153	4.92	1.02	0.0434	0.0040	0.1595	0.0124	168	3.3
115-1-15	105	199	6.13	0.46	0.0547	0.0042	0.1825	0.0117	161	3.3
115-1-16	123	211	6.56	1.11	0.0569	0.0047	0.1882	0.0137	157	3.1
115-1-17	116	221	6.69	0.57	0.0503	0.0040	0.1729	0.0123	158	2.9
115-1-18	82.9	169	5.39	1.00	0.0507	0.0047	0.1724	0.0140	166	3.7
115-1-19	97.1	192	6.01	0.87	0.0515	0.0047	0.1791	0.0134	162	3.6

Appendix: LA-ICP-MS Th-U-Pb analytical data of zircon

	Th 232 ppm	U 238 ppm	Pb Total ppm	Pb Common Pb ppm	$^{207}Pb/^{206}Pb$ Ratio	$^{207}Pb/^{206}Pb$ 1σ	$^{207}Pb/^{235}U$ Ratio	$^{207}Pb/^{235}U$ 1σ	$^{206}Pb/^{238}U$ Age (Ma)	$^{206}Pb/^{238}U$ 1σ(Ma)
P131-01	81.7	175	5.46	0.61	0.0502	0.0048	0.1742	0.0157	162	4.1
P131-02	148	228	7.03	0.11	0.0422	0.0040	0.1403	0.0124	161	3.1
P131-03	213	241	8.28		0.0479	0.0034	0.1648	0.0103	162	2.5
P131-04	140	218	6.91		0.0454	0.0033	0.1525	0.0098	159	2.8
P131-05	123	208	6.91	0.68	0.0490	0.0042	0.1787	0.0153	165	3.4
P131-06	124	205	6.55		0.0437	0.0034	0.1532	0.0103	164	3.0
P131-07	112	213	6.71	1.55	0.0534	0.0034	0.1827	0.0101	162	3.1
P131-08	99.6	183	5.84	1.87	0.0507	0.0036	0.1780	0.0114	165	3.0
P131-09	84.6	171	5.57	0.65	0.0524	0.0044	0.1859	0.0141	172	3.5
P131-10	254	218	7.66	3.66	0.0487	0.0038	0.1659	0.0115	159	2.7
P131-11	77.8	171	5.32	0.49	0.0527	0.0040	0.1880	0.0125	167	3.3
P131-12	113	215	6.71		0.0517	0.0035	0.1808	0.0104	166	2.8
P131-13	81.1	165	4.96		0.0582	0.0065	0.1840	0.0162	160	5.3
P131-14	94.8	172	5.60	9.82	0.0496	0.0041	0.1701	0.0124	165	3.2
P131-15	128	197	6.27	2.08	0.0533	0.0043	0.1864	0.0140	161	3.0
P131-16	95.9	139	4.51		0.0559	0.0065	0.1965	0.0177	161	4.0
P131-17	75.9	151	5.41	50.4	0.0518	0.0038	0.1892	0.0129	165	3.7
P131-18	126	217	6.85	0.74	0.0497	0.0035	0.1703	0.0103	161	2.8
P131-19	121	196	6.63	0.22	0.0516	0.0042	0.1919	0.0130	170	3.2

Appendix: LA-ICP-MS Th-U-Pb analytical data of zircon

	Th 232 ppm	U 238 ppm	Pb Total ppm	Pb Common Pb ppm	$^{207}Pb/^{206}Pb$ Ratio	$^{207}Pb/^{206}Pb$ 1σ	$^{207}Pb/^{235}U$ Ratio	$^{207}Pb/^{235}U$ 1σ	$^{206}Pb/^{238}U$ Age (Ma)	$^{206}Pb/^{238}U$ 1σ(Ma)
P132-1-01	173	256	8.39		0.0502	0.0040	0.1790	0.0127	165	3.0
P132-1-02	90.6	145	4.67		0.0485	0.0048	0.1615	0.0131	159	3.2
P132-1-03	117	210	6.68	1.48	0.0558	0.0039	0.1992	0.0134	164	3.3
P132-1-04	182	297	9.48	0.76	0.0593	0.0036	0.2073	0.0123	160	2.7
P132-1-05	107	191	6.05	1.83	0.0490	0.0042	0.1689	0.0133	159	3.0
P132-1-06	77.0	140	4.41	1.33	0.0622	0.0056	0.2111	0.0168	163	3.8
P132-1-07	107	176	5.47	1.58	0.0554	0.0060	0.1844	0.0184	156	3.2
P132-1-08	116	203	6.20	0.13	0.0513	0.0044	0.1815	0.0162	165	3.4
P132-1-09	144	224	7.31	1.02	0.0519	0.0037	0.1810	0.0112	163	3.0
P132-1-10	108	159	5.39	0.55	0.0523	0.0049	0.1847	0.0151	167	3.8
P132-1-11	102	186	6.05	0.50	0.0529	0.0055	0.1821	0.0173	160	4.0
P132-1-12	42.2	127	12.56	0.43	0.0561	0.0030	0.6341	0.0324	508	7.9
P132-1-13	85.9	147	5.03	1.03	0.0509	0.0047	0.1834	0.0136	171	4.0
P132-1-14	90.1	102	4.44		0.1689	0.0126	0.5842	0.0517	162	6.0
P132-1-15	171	252	8.70		0.0561	0.0040	0.2028	0.0132	169	3.3
P132-1-16	29.6	345	35.44	0.86	0.0744	0.0030	0.9319	0.0368	560	7.3
P132-1-17	127	216	6.96	0.45	0.0539	0.0041	0.1792	0.0117	161	3.2
P132-1-18	170	72.5	60.8		0.1664	0.0047	10.4220	0.2825	2411	25.9
P132-1-19	172	283	9.44	1.39	0.0522	0.0038	0.1919	0.0135	162	3.1
P132-1-20	10.8	31.9	3.19	1.53	0.0687	0.0103	0.8429	0.0998	604	20.7
P132-1-21	7.73	23.8	2.46		0.0727	0.0140	0.8205	0.1566	541	16.6
P132-1-22	88.7	189	5.84		0.0497	0.0040	0.1728	0.0124	162	3.2
P132-1-23	277	354	38.5	0.64	0.0469	0.0022	0.5402	0.0240	517	6.4